Solar Energy 286 (2025) 113145

Contents lists available at ScienceDirect

Solar Energy

journal homepage: www.elsevier.com/locate/solener

Simulation of shortwave infrared ratio thermometers for the remote opto-thermal characterisation of central external receivers

Simon Caron [a], Romain Larue [a], Andreas Kämpgen [b], Florian Sutter [a], Marc Röger [a], Michael Nieslony [a,*], Francisco Manzano-Agugliaro [c]

[a] Institute of Solar Research, German Aerospace Center (DLR), Calle Doctor Carracido 44-1, 04005 Almería, Spain
[b] CSP Services España S.L, Paseo de Almería, 73, 04001 Almería, Spain
[c] Department of Engineering, CEIA3, University of Almeria, 04120 Almería, Spain

ARTICLE INFO

Keywords:
Concentrated Solar Power
Solar Thermal
Infrared thermography
Absorber coating

ABSTRACT

The accurate knowledge of the receiver surface temperature T_{surf} is important for a safe, efficient and durable power plant operation. Its distribution is typically measured in real time using ground-based longwave infrared (LWIR) thermal cameras. Their calibration requires a priori knowledge of the receiver surface LWIR band emittance ε_{LWIR}. This parameter can be measured with great effort, using portable reflectometers for on tower optical inspection during periodical power plant maintenance. This paper analyses a new measurement principle, based on passive shortwave infrared (SWIR) ratio thermography, for the simultaneous measurement of surface temperature T_{surf} and band emittance ε_{SWIR}.

The first SWIR ratio thermometer combines two narrow bandpass filters centered on water vapor atmospheric absorption bands (1.4/1.9 μm). This thermometer is sensitive to water vapor to block solar radiation, however thermal radiation emitted by the receiver is also attenuated. The applicability of this thermometer is limited for remote opto-thermal characterization. Under favorable operating conditions, it can measure temperature leve[ls above 550 °C with a relative temperature error $\Delta T/T$ less than 2 %.

The second SWIR ratio thermometer combines two narrow bandpass filters centered on atmospheric windows (1.64/2.09 μm). This thermometer is insensitive to water vapor and suited for remote distances, however it can only operate off-sun when receiver surface temperature is still above 300 °C, for instance during the cool down phase, before molten salts drainage. The relative temperature error $\Delta T/T$ is less than 0.5 % for Pyromark 2500 and oxidized Haynes 230, while the absolute band emittance error $\Delta\varepsilon$ is less than 2.5 percentage points.

1. Introduction

Solar energy is the largest energy resource available on Earth, capable of meeting several times the global primary energy demand [1]. Photovoltaics (PV) and Concentrated Solar Power (CSP) are two relevant technologies for solar energy conversion [2,3]. While the worldwide installed PV capacity has reached 1 TW_p in 2022 [4], CSP technology is yet at an earlier stage of deployment, with an installed capacity of ∼ 7 GW_e [5]. Multiple hybrid power plants, combining, CSP, PV/Wind and thermal storage are being planned and constructed in China [6]. While CSP technology may play a marginal but critical role in the stabilization of electrical grids, it should contribute in the decarbonization of Industrial Process Heat (IPH) and the production of synthetic fuels [7–10], especially for high temperature processes which are more challenging for direct electrification. In addition to synthetic fuel production, the field of solar thermochemistry encompasses various additional kinds of chemical applications of high temperature solar energy, such as the production of hydrogen and chemical commodities, carbon dioxide capture and thermochemical heat storage at high temperatures [11–13].

CSP systems use a tracking mirror field to focus sunlight on a thermal receiver. A Heat Transfer Fluid (HTF) is circulated through the thermal receiver in a primary loop. The collected heat is transferred to any thermal process and to a thermal storage unit. The mirror field can be arranged in a line focusing (LF) or a point focusing (PF) configuration. LF systems, such as Parabolic Trough Collectors (PTC) [14] or Linear Fresnel collectors [15], use single axis trackers to focus solar radiation on linear receivers. PF systems, such as Central Receiver Systems (CRS) [16], use two axis trackers, also known as heliostats, to focus solar radiation on a surface, for instance an external cylindrical receiver

* Corresponding author.
E-mail address: michael.nieslony@dlr.de (M. Nieslony).

https://doi.org/10.1016/j.solener.2024.113145
Received 6 December 2023; Received in revised form 30 September 2024; Accepted 25 November 2024
Available online 17 December 2024

Nomenclature

Abbreviations

AM	Air Mass
ARC	Anti-Reflection Coating
AFD	Allowable Flux Density
BF	Blackbody calibration function
COTS	Commercial of the Shelf
CRS	Central Receiver System
CSP	Concentrated Solar Power
DOE	Design of Experiments
DMP	Double Modulation Pyrometry
FAMP	Flash Assisted Multiwavelength Pyrometry
GF	Greybody calibration function
HTF	Heat Transfer Fluid
IPH	Industrial Process Heat
IR	Infrared
LCOC	Levelized Cost of Coating
LF	Line Focusing
LW	Longwave (8—14 μm)
m.a.s.l.	Meters above sea level
MLS	Mid Latitude Summer
MODTRAN	MODerate resolution atmospheric TRANsmission
MW	Midwave (3—5 μm)
NB	Narrow Bandpass
NIST	National Institute of Standards and Technology
NUC	Non-Uniformity Correction
PF	Point Focusing
PTC	Parabolic Trough Collector
PV	Photovoltaics
SH	Sakuma-Hattori
SOC	Surface Optics
SPTC	Solar Power Tower Check
SRF	Spectral Response Function
SW	Shortwave (1 – 2.5 μm)

Universal physical constants

c_0	Speed of light in vacuum[m.s^{-1}]
h	Planck's constant[J.s]
k	Boltzmann's constant[J.K^{-1}]
σ	Stefan-Boltzmann constant[W.m^2.K^{-4}]

English symbols

A_1	Sakuma Hattori fit coefficient[W.m^{-2}]
A_2	Sakuma Hattori fit coefficient[K^{-1}]
AH	Absolute Humidity[g.m^{-3}]
B_1	Greybody ratio fit coefficient[K^{-1}]
B_2	Greybody ratio fit intercept[-]
C_x	Concentration factor[-]
CWL	Central wavelength[μm]
d	Distance[km]
E	Spectral irradiance[W.m^{-2}.μm^{-1}]
I	Radiometric signal[W.m^{-2}]
FWHM	Full Width at Half Maximum[μm]
NGCF	Non-Grey Compensation Factor[-]
OD	Optical Depth[-]
P	Pressure[mbar]
QE	Quantum Efficiency[%]
RH	Relative Humidity[%]
S	Radiometric signal[W.m^{-2}]
SR	Signal Ratio[-]
SZA	Solar Zenith Angle[°]
T	Temperature[°C, K]

Greek symbols

α	Absorptance[%]
ε	Emittance[%]
Δ	Difference[-]
λ	Wavelength[μm]
η	Efficiency[%]
τ	Transmittance[%]
ρ	Reflectance[%]
Θ	Incidence angle[°]

English subscripts

atm	Atmosphere
band	Bandpass filter
bb	Blackbody
cam	Camera
detector	Detector
filter	Filter
lens	Objective lens
mirror	Mirror
opt-th	Opto-thermal
path,i	Atmospheric path (1,2,3)
peak	Peak
sensor	Sensor
sun	Sun
surf	Receiver surface
{x,y}	Pixel
window	Protective window

mounted at the top of a tower. In comparison to LF systems, PF systems can achieve a higher concentration factor C_x, significantly above x100. Higher concentration factors lead to higher HTF operating temperatures, above 600 °C, and thus a higher thermodynamic efficiency [17].

External receivers [18,19] are made of high temperature metal alloys, such as nickel–chromium superalloys. The receiver surface is coated with an absorber coating, such as Pyromark 2500 [20–22] or alternative black paints [23–25]. These absorber coatings have very high spectral absorptance values generally well above 90 % in the visible and shortwave (SW) infrared wavelength range in order to maximize the absorbed solar irradiance [26].

The thermal receiver is subject to high flux densities in operation, up to 1 MW/m^2 and local molten salt temperatures above 600 °C, potentially inducing severe metal corrosion [27]. These constraints may lead to critical thermomechanical damages and reduced service lifetime [28]. Allowable Flux Densities (AFD) are thus defined for a safe receiver operation [29], requiring optimal aiming strategies for the heliostat field [30,31]. There is a variety of techniques to measure the flux density levels on the receiver surface in order to stay within the AFD limits, for example with remote CCD camera measurement configurations [32] or with water-cooled Lambertian targets in the measurement plane [33].

The absorber coating is also subject to cyclic thermal stresses during operation, impacting its opto-thermal efficiency $\eta_{opt\text{-}th}$ and durability [21–25,34–37]. The key figures of merit affecting $\eta_{opt\text{-}th}$ are primarily the solar absorptance α_{sol} and secondarily the thermal emittance ε_{th} [38,39]. The porous coating may crack and delaminate, uncovering an oxide layer, with a lower $\eta_{opt\text{-}th}$ value [21,34,37]. A periodical recoating of the receiver surface may be considered, optimizing the Levelized Cost of Coating (LCOC) [40,41].

The safe, efficient and durable operation of the central external receiver requires monitoring its surface temperature and the absorber coating health status. An accurate temperature measurement and control of the receiver surface allows an efficient CRS operation, while it may prevent coating degradation and more critical thermomechanical damages of the receiver.

Conventional temperature monitoring techniques include for example the use of contact sensors or pyrometers in order to estimate the temperature of receiver surfaces. [33]. Contact sensors such as thermocouples provide the advantage of directly measuring temperatures and therefore do not require any information about the spectral emittance of the receiver material or the amount of reflected radiation from the receiver surface. However, it is not possible to place them on the front side of the receiver since the measured temperature will not be correct due to the absorbed solar radiation. A measurement at the back of the receiver is possible, but tied to a reduced accuracy of the temperature measurements [42]. In the case of pyrometry approaches, usually so-called solar-blind pyrometric measurement systems [43] are used to decouple the thermally emitted radiation from the reflected radiation from the heliostat field. Both the measurement with contact sensors as well as pyrometers delivers temperature values for single measurement points while usually the temperature distribution across the whole receiver surface is of interest. [44]. In this context, remote thermography approaches are quite interesting because they are contact-free and deliver a spatially resolved temperature profile. The main challenge for thermography approaches is the disentanglement of the temperature and emissivity measurement of the receiver surface, which can be overcome by applying ratio thermometry, i.e. measuring the ratio of radiation signals at different wavelength ranges.

The aim of this paper is to analyse a new measurement principle based on SW infrared (IR) ratio thermometry, designed for the remote opto-thermal characterization of central external receivers, i.e. a simultaneous measurement of surface temperature and band emittance. The measurement technique works on external receiver surfaces, but is not applicable to cavity type receivers. An industrially relevant external receiver for which SW IR ratio thermometry might be particularly interesting is the molten salt receiver, often constructed in cylindrical form. Existing field measurement instruments and scientific measurement concepts are reviewed in the first section. The new measurement principle is then described in the next section. The modelling approach used for the evaluation of this measurement principle is presented in the third section. Simulation results for two SWIR ratio thermometer configurations are then discussed in the fourth section.

2. State of the art

2.1. Measurement instruments

Two types of measurement instruments are used in the field for CRS opto-thermal monitoring. On the one hand, Longwave (LW) IR thermography (8–14 μm) is used for mapping and monitoring the receiver surface temperature T_{surf} from the ground in real time during operation. On the other hand, portable devices, such as a solar reflectometer and an emissometer can be used for an optical inspection of the receiver coating on tower during periodical maintenance. The solar reflectometer measures the solar absorptance α_{sol}, while the emissometer measures the thermal emittance ε_{th} or a surface band emittance $\varepsilon_{surf,band}$ for a specific IR spectral range. A set of Commercially Off-The-Shelf (COTS) available instruments [45,46] is illustratively shown in Fig. 1. Their key specifications are outlined in Table 1.

2.1.1. LWIR thermography

For external receiver designs, multiple LWIR camera units (Fig. 1.a.) are located on the ground around the receiver circumference for a redundant monitoring from different perspectives. The typical view angle of the receiver is about 45°. As the receiver height can be above 200 m, industrial LWIR cameras with a high resolution (1024x768 pixels) are combined with custom teleobjectives, made of Germanium lenses with anti-reflective coating (ARC), with a focal length above 200 mm in order to resolve single tubes. Each LWIR camera unit uses an uncooled micro-bolometer as a detector and is mounted inside an athermalized protective housing, with a protective window made of Germanium with ARC, to minimize the influence of outdoor conditions, such as solar radiation or ambient temperature, on the temperature measurement accuracy.

LWIR camera units monitor the receiver surface temperature in real time through all operation phases during the day, in particular when molten salts are filled and drained in the central receiver [47]. These phases are particularly important to avoid critical molten salt freezing below 250 °C. Furthermore, LWIR temperature maps are coupled to the power plant control system and can be used for inverse flux

Table 1
Key instrumentation specifications for CRS monitoring.

Specification	LWIR thermography	Solar reflectometer	Emissometer
Device model	Infratec SPTC [45]	SOC 410-Solar [46]	SOC ET100 [46]/ ET10
Spectral range	LWIR Broadband Band: 7.5 – 14 μm	UV–VIS-SWIR 6 spectral bands 0.335 – 2.5 μm	IR (SW, MW, LW) 7 spectral bands ET100: 1.5 – 21 μm ET10: 3–5 μm / 8–12 μm
Resolution	Pixel matrix	Point measurement	Point measurement
Measurand	Surface temperature map from −40 °C up to 2000 °C	α_{sol}	ET100: ε_{th} ET10: $\varepsilon_{surf,band}$
Operation mode	Continuous Ground based	Periodical maintenance On tower, T_{amb}	Periodical maintenance On tower, T_{amb}
Calibration inputs	Surface band emittance: $\varepsilon_{surf,band}$ Atmospheric transmittance: $\tau_{atm,band}$	NIST traceable calibration coupon (white diffuse)	NIST traceable calibration coupon (gold diffuse)

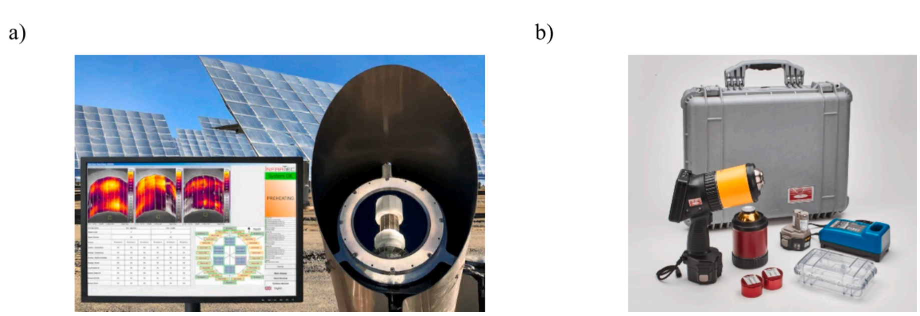

Fig. 1. Field Instrumentation for CRS monitoring a) Thermographic Monitoring (LWIR) of Solar Power Tower (Infratec SPTC) [45] b) Surface Optics (SOC) portable 410-Vis-IR solar reflectometer and emissometer [46].

measurements using a receiver thermodynamic model and thus adjusting the aiming point control strategy of the heliostat field [48,49].

The calibration of LWIR camera systems require some a priori knowledge from the operators. On the one hand, the band emittance $\varepsilon_{surf,band}$ of the receiver surface must be estimated, considering potential non-uniformities due to local coating degradation. This calibration may be achieved off-sun at the end of the day, when the receiver cools down and is maintained at an isothermal temperature around 300 °C before molten salts are drained. This calibration method assumes that $\varepsilon_{surf,band}$ is not temperature dependent [50]. On the other hand, the atmospheric band transmittance $\tau_{atm,band}$ must be estimated for the slant path between the camera and the receiver. This parameter is primarily a function of distance d, ambient temperature T_{amb} and relative humidity RH. Empirical correlations based on radiative transfer codes are typically used for this estimation [51].

While LWIR thermography is robust for industrial applications, there are currently some practical obstacles to improve the calibration traceability of such measurement systems in the context of CRS applications. The spectral response of the LWIR optical system is for instance seldom provided for radiometric simulations. The thermography software may also not allow the end user to access the calibration function or the radiometric chain, impeding the direct comparison of radiometric quantities.

2.1.2. Portable instruments

Portable instruments (Fig. 1.b) allow performing an in-situ optical inspection of the receiver surface at ambient temperature, comparable with laboratory spectrophotometers [39]. A modular measurement head includes an integrating sphere, with a discretized spectral resolution (Fig. 2), adjusted for the selected measurand, e.g. α_{sol}, ε_{th} or $\varepsilon_{surf,band}$. Solar absorptance measurements are for instance used to decide whether re-coating should occur, defining a lower threshold such as 95 % for α_{sol} [24].

While the 410-Vis-IR instrument is already known in the CSP community, there is no experience with the ET-10 measurement head, which could allow a ground truthing for LWIR thermography, assuming a comparison of spectral responses is possible for both instruments. One practical disadvantage of such portable instrument is the necessity for operators to climb on tower, above 200 m, during periodical power plant maintenance.

2.2. Measurement techniques

Different measurement techniques in radiation thermometry have been previously implemented and tested in the field of CSP and other research applications. These measurement techniques can be classified according to:

i) the selected IR spectral band and its sensitivity to solar radiation (*solar blindness*)
ii) the number N of spectral bands used for measurements (*Multi-spectral thermometry*)
iii) the active use of light sources during measurements (*passive vs. active techniques*)

2.2.1. Solar blindness

The choice of the IR spectral bandwidth is particularly critical, as concentrated solar radiation may hamper the temperature measurement accuracy. So-called "solar-blind" temperature measurements have been performed in solar furnaces [52–54] and on parabolic trough receivers and volumetric absorbers [55,56]. Solar blindness can be achieved with different approaches, after a thorough analysis of the specific radiometric chain [52]:

i) selecting a Narrow Bandpass (NB) filter centered on an atmospheric absorption band, such as 1.4 µm (H_2O), 1.9 µm (H_2O), 2.7 µm ($H_2O + CO_2$), 4.3 µm ($H_2O + CO_2$).
ii) selecting a spectral range where the mirror specular reflectance is minimal ($\rho_{mirror} \sim 0$)
iii) temporarily occulting concentrated solar radiation while maintaining temperature ($C_x = 0$)
iv) achieving blackbody conditions for the receiver surface ($\varepsilon_{surf,band} \sim 1$).

One can further distinguish near and true solar-blind temperature measurements. The accuracy of near solar-blind temperature measurements depends on atmospheric conditions, such as Air Mass (AM) or Solar Zenith Angle (SZA) and operating conditions, such as concentration factor C_x and surface temperature T_{surf}. True solar-blind temperature measurements can only be guaranteed if the reflection of the concentrated solar flux is totally cancelled by at least one component of the radiometric chain.

For atmospheric absorptions bands, near solar-blind temperature measurements are achieved at 1.4 and 1.9 µm, while true solar-blind temperature measurements are achieved at 2.7 and 4.3 µm. Nonetheless, the atmosphere does not only attenuate the concentrated solar radiation, but also the thermal radiation emitted by the receiver surface. For central external receivers, near solar-blind temperature measurements can be assumed for LWIR thermometry, as the applied black coating approximates a blackbody. Operating conditions are also less extreme in comparison to solar furnace. For molten salts, the surface temperature should not exceed 600 °C and the maximum flux is about 1 MW/m^2 [19].

2.2.2. Multi-spectral thermometry

IR thermography can be performed with a single spectral band ($N =$

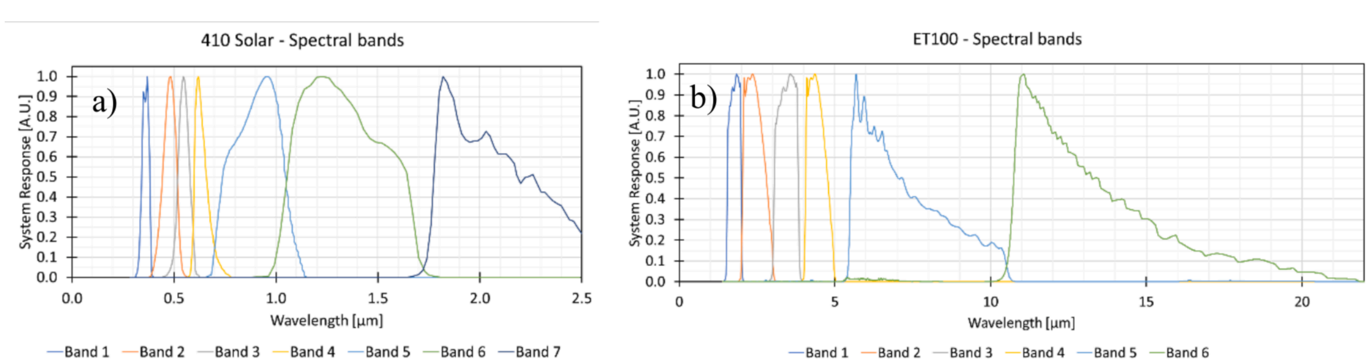

Fig. 2. Spectral response of portable instrument measurement heads in arbitrary units. a) 410 Solar reflectometer (0.33—2.5 µm). b) ET100 emissometer (1.5 – 21 µm).

1) or with multiple spectral bands. For single band thermography, a priori knowledge is required for the surface band emittance $\varepsilon_{surf,band}$ and the atmospheric band transmittance $\tau_{atm,band}$. A variant is ratio thermometry ($N = 2$), combining two spectral bands and assuming a grey behavior for the investigated material, i.e. a constant surface band emittance $\varepsilon_{surf,band}$ and atmospheric band transmittance $\tau_{atm,band}$ for the spectral range of interest [57–59]. The grey assumption may be corrected with a Non-Grey Compensation Factor (NGCF) [60].

Ratio thermometry allows a simultaneous retrieval of a material surface temperature T_{surf} and its band emittance $\varepsilon_{surf,band}$. Published references have focused on short ranges and wavelengths for which the influence of atmospheric band absorption can be considered negligeable ($\tau_{atm,band} \sim 1$). Due to blackbody radiation physics, ratio thermometry is more sensitive for SWIR (1–2.5 μm) than for Midwave (MW; ~ 3–5 μm) or LW (~ 8–14 μm) IR spectral ranges.

Although multi-spectral thermometry ($N > 2$) exists, it always results in an ill-posed problem with an underdetermined system of equations [61]. There are $N + 1$ unknown for N band measurements: N unknown for each spectral band emittance $\varepsilon_{surf,band}$ and one unknown for the surface temperature T_{surf}. A relationship between emissivity and wavelength has to be assumed, with inherent mathematical difficulties [62].

2.2.3. Passive versus active techniques

Passive radiation thermometry concepts exploit only the thermal radiation emitted by the surface for temperature measurements. Active radiation thermometry concepts combine one or several modulated light sources in addition of the radiation thermometer, to extract more information on the surface optical properties. Active radiation thermometry concepts include:

i) Two-color pyroreflectometry [63–65]
ii) Flash-Assisted Multiwavelength Pyrometry (FAMP) [66,67]
iii) Double Modulation Pyrometry (DMP) [68–71]

These active measurement techniques, originally developed for pyrometry, could be extended in spatial resolution for thermography [72,73].

Two-color pyroreflectometry is a variant of passive ratio thermometry. It measures simultaneously the sample surface radiance temperature and its reflectivity, retrieving the surface true temperature T_{surf}, introducing a diffusion factor, which is assumed independent of wavelength λ. This technique operates at two different close wavelengths, for instance at 1.3 and 1.55 μm, using corresponding NB filters and wavelength compatible modulated light sources.

The FAMP technique measures in-situ the spectral reflectance of a lambertian sample, its temperature and the spectral irradiance of the light source by measuring twice the spectral contents of the light from the sample and from a cooled reflectance reference situated nearby. Two measurements are made sequentially, one with and one without additional light from an external flash.

The DMP technique has been originally developed for artificial solar furnaces, where solar blind pyrometry is not applicable due to the arc lamp continuous spectrum. It relies on a single color pyrometric method and thus requires a priori knowledge of the sample band emittance. This technique allows separating the external reflection radiation reflected by a sample from its thermal emission, by modulating the light source.

While active measurement techniques have been successfully experimented at laboratory scale, they are probably difficult to scale for a ground-based temperature measurement of a central external receiver. Furthermore, the addition of modulated light sources increases the complexity of the temperature measurement system.

3. Measurement principle

The scope of this paper focuses on the analysis of two passive SWIR ratio thermometers for the ground-based measurement of central external cylindrical receiver surface temperature T_{surf} and band emittance $\varepsilon_{surf,band}$. Two configurations are considered for simulation:

i) a near solar blind configuration for on-sun measurements, combining two NB filters centered on two neighbor SWIR atmospheric water absorption bands, i.e. 1.4 μm and 1.9 μm
ii) an alternative configuration for off-sun measurements, combining two NB filters centered on two neighbor SWIR atmospheric windows, i.e. 1.64 μm (H band) and 2.09 μm (K band) [74].

This section describes the radiometric chain for central external receivers, the rationale for applying ratio thermography and the spectral configuration of the prototype camera system.

3.1. Radiometric chain

The radiometric chain for the ground-based thermography of central external receivers is illustrated in Fig. 3. The IR camera is mounted on the ground at a height H_0 (m.a.s.l.) within the heliostat field and looks at one receiver section on top of the tower at a height H above the ground. The measurands of interest for opto-thermal characterization are the surface temperature map T_{surf}(x,y) and the surface band emittance map $\varepsilon_{surf,band}(x,y)$.

The radiometric chain consists of three main atmospheric paths, assuming an equivalent heliostat, which is representative for the heliostat field:

4. Path 1: Sun to heliostat (slant distance d_1, function of Air Mass AM).
5. Path 2: Heliostat to receiver (slant distance d_2).
6. Path 3: Receiver to IR camera (slant distance d_3).

A ground-based weather station give access to parameters such as atmospheric pressure P_{atm}, ambient temperature T_{amb} and relative humidity RH. This information is used to parametrize the atmospheric model, in particular water vapor content. One relevant unit is absolute humidity AH [g/m^3] at ground level, computed using Vaisala humidity conversion formulas [75].

The ground-based IR camera detects a radiometric signal S, which sums three contributions, i.e.:

i) Term A: Thermal radiation emitted by the diffuse receiver surface
ii) Term B: Reflected concentrated solar radiation
iii) Term C: Thermal radiation emitted by the atmosphere

The IR camera detector may also detect its own thermal radiation reflected by the filter (Term D) [76].

A radiometric equation is formulated for the detected spectral irradiance $I_{\{x,y\}}(\lambda)$ [W.m^{-2}.μm^{-1}] (Eq.1), for any pixel $\{x,y\}$ and wavelength λ. This radiometric equation can be further integrated bandwise (Eq.2) for any given NB filter over the spectral range [λ_{start}; λ_{stop}] to yield a camera signal $S_{\{x,y\}}$(filter).

$$I_{\{x,y\}}(\lambda) = A_{\{x,y\}}(\lambda) + B_{\{x,y\}}(\lambda) + C_{\{x,y\}}(\lambda) + D_{\{x,y\}}(\lambda) \tag{1}$$

$$S_{\{x,y\}}(\text{filter}) = \int_{\lambda_{start}}^{\lambda_{stop}} I_{\{x,y\}}(\lambda).d\lambda \tag{2}$$

Terms A,B,C and D are explicited further in (Eq. 3–6), omitting the pixel notation for readability:

$$A(\lambda) = \varepsilon_{surf}(\lambda).\tau_{atm,path3}(\lambda, d_3, \text{atm}).E_{bb}(\lambda, T_{surf}).\text{SRF}_{cam}(\lambda, T_{cam}) \tag{3}$$

$$B(\lambda) = C_x.[1 - \varepsilon_{surf}(\lambda)].\left[\prod_{i=1}^{3} \tau_{atm,path(i)}(\lambda, d_i, \text{atm})\right].\rho_{mirror}(\lambda).\cos(\theta).E_{sun}(\lambda, \text{AM0}).\text{SRF}_{cam}(\lambda, T_{cam}) \tag{4}$$

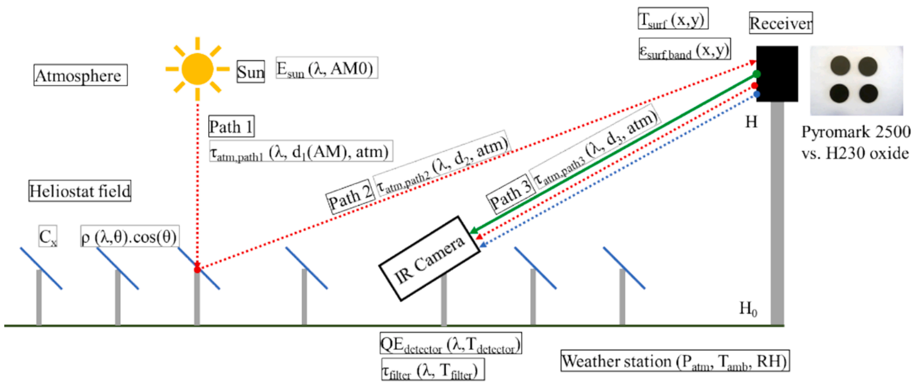

Fig. 3. Radiometric chain for ground-based thermography of central external receivers.

$$C(\lambda) = \left[1 - \tau_{\text{atm,path3}}(\lambda, d_3, \text{atm})\right].E_{\text{bb}}(\lambda, T_{\text{atm}}).\text{SRF}_{\text{cam}}(\lambda, T_{\text{cam}}) \tag{5}$$

$$D(\lambda) = \left[1 - \tau_{\text{filter}}(\lambda, T_{\text{filter}})\right].E_{\text{bb}}(\lambda, T_{\text{sensor}}).\text{QE}_{\text{sensor}}(\lambda, T_{\text{sensor}}) \tag{6}$$

The function $E_{bb}(\lambda,T)$ is defined by Planck's law of blackbody radiation (Eq. 7).

$$E_{\text{bb}}(\lambda, T) = \frac{2\pi.h.c_0^2}{\lambda^5\left[\exp\left(\frac{h.c_o}{\lambda.k.T}\right) - 1\right]} \tag{7}$$

The camera spectral response function f_{cam} (λ,T_{cam}) is defined by (Eq. 8).

$$\text{SRF}_{\text{cam}}(\lambda, T_{\text{cam}}) = \tau_{\text{window}}(\lambda, T_{\text{window}}).\tau_{\text{lens}}(\lambda, T_{\text{lens}}).\tau_{\text{filter}}(\lambda, T_{\text{filter}}).\text{QE}_{\text{sensor}}(\lambda, T_{\text{sensor}}) \tag{8}$$

The extraterrestrial solar spectrum E_{sun} $(\lambda,\text{AM0})$ and atmospheric transmittance spectra $\tau_{atm,path(i)}$ are generated with MODTRAN6 radiative transfer code [77,78]. For simulations, a reference mirror spectrum $\rho_{mirror}(\lambda,\Theta)$ is considered for a near normal incidence angle, assuming there is no soiling or degradation. Although the heliostat field deflects solar radiation on the receiver, the cosine effect $(\cos(\Theta))$ is here assumed negligible for simplification.

The measurands of interest, i.e. T_{surf} and ε_{surf}, are embedded in term A (Eq.3). The surface emittance ε_{surf} is also embedded in term B (Eq.4). To extract T_{surf} and ε_{surf} measurands, it is necessary to isolate term A (Eq.3). The radiometric equation (Eq.1) simplifies considerably if terms B, C and D could be considered negligeable.

Term B (Eq. 4) is negligible only under near or true solar blind conditions. This can be achieved in practice by selecting NB filters centered around atmospheric water absorption bands, for instance 1.4 µm and 1.9 µm. In this case, the aim is to cancel $\tau_{atm,path1}$, by finding suitable atmospheric conditions (AH,AM) and operating conditions (C_x, T_{surf}) which minimize the expected temperature error. Nonetheless, atmospheric water vapor also affects path 3, i.e. the atmospheric attenuation $\tau_{atm,path3}$ between the receiver and the camera [79,80]. Another strategy is to work off-sun ($C_x = 0$), when heliostats are defocused and the receiver cools down at dusk. NB filters centered in atmospheric windows, for instance 1.64 µm and 2.09 µm are significantly less affected by atmospheric conditions.

Term C (Eq. 5) is generally negligible, as long as the atmosphere temperature T_{atm} is significantly lower than the receiver surface temperature T_{surf}. Term D is camera specific, generating a signal offset. It can become negligible, depending on the spectral range and the camera sensor temperature. This may be a potential issue for LWIR cameras (8–14 µm) using an uncooled microbolometer with inadequate athermalization [76]. For a SWIR camera, this is not critical as the sensor can be cooled down below ambient temperature using thermoelectric cooling, to reduce dark current noise.

3.2. Ratio thermometry

Assuming the object thermal emission can be expressed (Eq.9) for a given NB filter:

$$S(\text{filter}) \approx \int_{\lambda_{\text{start}}}^{\lambda_{\text{stop}}} \varepsilon_{\text{surf}}(\lambda).\tau_{\text{atm,path3}}(\lambda, d_3, \text{atm}).E_{\text{bb}}(\lambda, T_{\text{surf}}).\text{SRF}_{\text{cam}}(\lambda, T_{\text{cam}}).d\lambda \tag{9}$$

This equation can be expressed in lumped form after integration (Eq.10):

$$S(\text{filter}) \approx \varepsilon_{\text{surf}}(\text{filter}).\tau_{\text{atm,path3}}(\text{filter}).\text{BF}(\text{filter}, T_{\text{surf}}) \tag{10}$$

Where the band surface emittance ε_{surf}(filter) and the band atmospheric transmittance $\tau_{atm,path3}$(filter) are respectively defined in (Eq.11–12) and the NB filter blackbody calibration function in (Eq.13).

$$\varepsilon_{\text{surf}}(\text{filter}) = \frac{\int_{\lambda_{\text{start}}}^{\lambda_{\text{stop}}} \varepsilon_{\text{surf}}(\lambda).E_{\text{bb}}(\lambda, T_{\text{surf}}).\text{SRF}_{\text{cam}}(\lambda, T_{\text{cam}}).d\lambda}{\text{BF}(\text{filter}, T_{\text{surf}})} \tag{11}$$

$$\tau_{\text{atm,path3}}(\text{filter}) = \frac{\int_{\lambda_{\text{start}}}^{\lambda_{\text{stop}}} \tau_{\text{atm,path3}}(\lambda, d_3, \text{atm}).E_{\text{bb}}(\lambda, T_{\text{surf}}).\text{SRF}_{\text{cam}}(\lambda, T_{\text{cam}}).d\lambda}{\text{BF}(\text{filter}, T_{\text{surf}})} \tag{12}$$

$$\text{BF}(\text{filter}, T_{\text{surf}}) = \int_{\lambda_{\text{start}}}^{\lambda_{\text{stop}}} E_{\text{bb}}(\lambda, T_{\text{surf}}).\text{SRF}_{\text{cam}}(\lambda, T_{\text{cam}}).d\lambda \tag{13}$$

The blackbody calibration function BF (Eq.13) can be simulated knowing the camera spectral response SRF_{cam} or measured in laboratory with a reference blackbody ($\varepsilon > 0.99$), assuming the effect of atmospheric transmittance is properly considered. The BF function can be further inverted, preferably in analytical form, to obtain the reciprocal function between the temperature T and the sensor signal S ($T = \text{BF}^{-1}(S)$). Various equations were proposed by Sakuma and Hattori [81].

For a single band thermometer, a priori knowledge of $\varepsilon_{surf,band}$ and $\tau_{atm,band}$ is required to infer the surface temperature T_{surf}. While $\tau_{atm,path3,band}$ could be derived from model-based correlations [51] using atmospheric radiative transfer codes such as MODTRAN [77,78], $\varepsilon_{surf,band}$ may be derived from laboratory measurements performed at high temperature [50], if available.

A ratio thermometer requires a pair of NB filters {filter 1; filter 2}. The signal ratio SR is defined as the ratio of signals obtained for each NB filter (Eq.14):

$$\text{SR} = \frac{S(\text{filter 2})}{S(\text{filter 1})} \approx \frac{\varepsilon_{\text{surf}}(\text{filter 2})}{\varepsilon_{\text{surf}}(\text{filter 1})}.\frac{\tau_{\text{atm,path3}}(\text{filter 2})}{\tau_{\text{atm,path3}}(\text{filter 1})}.\frac{\text{BF}(\text{filter 2}, T_{\text{surf}})}{\text{BF}(\text{filter 1}, T_{\text{surf}})} \tag{14}$$

Using a pair of NB filters provides two independent band measurements for three unknowns, i.e. the $\varepsilon_{surf}.\tau_{atm,path3}$ product for each NB filter and the surface temperature T_{surf}. The equation system is thus underdetermined, without any a priori knowledge. While the atmospheric band transmittance ratio can be estimated using a radiative transfer code, a further assumption is required for the surface band emittance ratio.

The principle of ratio thermometry [57–61] relies on the greybody assumption (Eq.15). This requires selecting a pair of NB filters with central wavelengths (CWLs) chosen as close as possible to consider valid the greybody assumption, but not too close, otherwise redundant signals are measured and the equation system remains underdetermined.

$$\frac{\varepsilon_{surf}(\text{filter }2)}{\varepsilon_{surf}(\text{filter }1)} \ 1; \varepsilon_{surf,band} = \varepsilon_{surf}(\text{filter }1) = \varepsilon_{surf}(\text{filter }2) \tag{15}$$

The greybody approximation is considered relevant for the selected spectral range and for the materials of interest, i.e. Pyromark 2500 black coating or oxidized Haynes 230 (H230) metal substrate, as illustrated in Fig. 4. Both materials also have a high spectral emittance, near or above 90 %.

On the other hand, the greybody approximation is not necessarily valid for the atmosphere. A model based atmospheric NGCF is introduced for correction (Eq.16).

$$\text{NGCF}_{atm} = \frac{\tau_{atm,path3}(\text{filter }2)}{\tau_{atm,path3}(\text{filter }1)}; \text{NGCF}_{atm} \neq 1 \tag{16}$$

The ratio of blackbody calibration functions [BF(filter 2,T_{surf})/BF(filter 1,T_{surf})] defines an ancillary greybody calibration function GF(T_{surf}) (Eq.17):

$$\text{GF}(T_{surf}) = \frac{\text{BF}(\text{filter }2, T_{surf})}{\text{BF}(\text{filter }1, T_{surf})} \tag{17}$$

In practice, the retrieval of the surface temperature T_{surf} and band emittance $\varepsilon_{surf,band}$ occurs stepwise. The NGCF_{atm} is estimated based on available weather data at ground level. Assuming a greybody receiver surface, the measured signal ratio SR is divided by NGCF_{atm}. The greybody calibration function GF(T_{surf}) is then inverted to infer the surface temperature T_{surf}. Knowing this temperature, the measured signal for each NB filter is divided by the corresponding blackbody temperature signal (BF(filter,T_{surf})) to obtain first the $\varepsilon_{surf}.\tau_{atm,path3}$ product for each NB filter, then the surface band emittance $\varepsilon_{surf,band}$, as $\tau_{atm,path3}$ is already estimated for NGCF_{atm}.

3.3. Camera configuration

The prototype SWIR camera system consists of the following components:

i) A C16090-03 module (Hamamatsu) with an InGaAs image sensor (G14673-0808 W) [82]
ii) A motorized filter wheel with six filter positions
iii) A set of stock available NB filters supplied by Spectrogon [83]
iv) A SWIR objective lens with a 300 mm focal length [84]

The camera system is mounted inside an outdoor protection housing with a Gorilla glass window of 2 mm thickness. Four positions of the filter wheel are used for NB filters of 1 mm thickness, while two filter positions are used for a shutter and a broadband window. The shutter and broadband window can be used for Non-Uniformity Correction (NUC). The broadband window also allows focusing the camera system on remote objects at ambient temperature.

Selected NB filters are listed in Table 2. Two pairs of NB filters are considered as SWIR ratio thermometers. The first SWIR ratio thermometer is sensitive to water vapor and should allow near solar blind measurements, while the second SWIR ratio thermometer is minimally sensitive to atmosphere, but definitely not solar blind.

The spectral response of each relevant optical component (sensor, objective lens, NB filters, protective window) is shown in Fig. 5. The image sensor is cooled at −20 °C, while other components are at ambient temperature. Virtual blackbody calibration curves are shown for each NB filter in Fig. 6.a, while virtual greybody calibration curves are shown for each ratio thermometer in Fig. 6.b.

Virtual blackbody filter calibrations (Fig. 6.a) can be fitted with a Sakuma-Hattori (SH) Planck 1 equation [81] (Eq.18), while virtual greybody ratio calibrations (Fig. 6.b) can be fitted with a log-linear model (Eq.19), considering the inverse of the temperature T. In both equations, the temperature must be expressed in Kelvins.

$$\text{BF}(T) = \frac{A_1}{\exp\left(\frac{A_2}{T}\right) - 1} \tag{18}$$

$$\text{GF}(T) = \exp\left(\frac{B_1}{T} + B_2\right) \tag{19}$$

Virtual blackbody calibration fitted coefficients are listed in Table 3 for each NB filter, while virtual greybody calibration fitted coefficients are listed in Table 4 for each ratio thermometer.

4. Modelling approach

A MATLAB software tool has been developed for the spectral simulation of the radiometric chain described in Section 3.1, in order to analyse ratio thermometers described in Sections 3.2 and 3.3. The software tool consists of two steps, i.e. a forward problem and an inverse problem, presented in the next subsections. The last subsection describes the batch simulation setup.

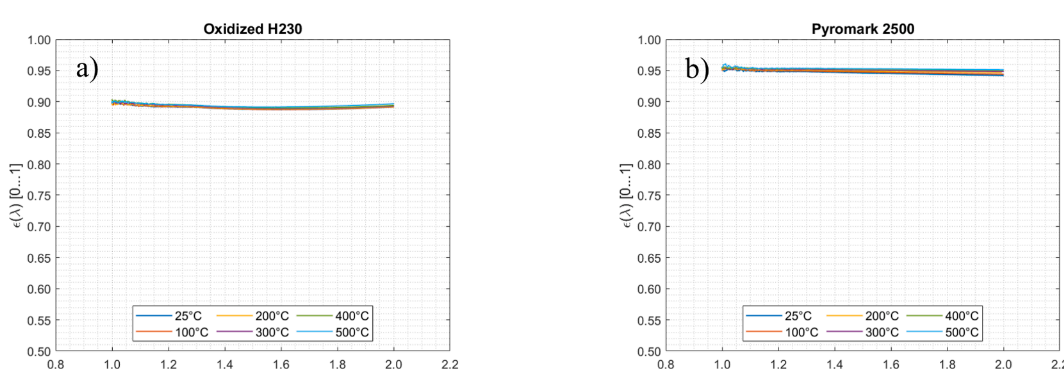

Fig. 4. SWIR spectral measurements of reference materials from ambient temperature up to 500 °C. a) H230, pre-oxidized at 800 °C for 100 h. b) Pyromark 2500 applied on H230 substrate.

Table 2
Specifications of NB filters for SWIR ratio thermography.

Filter ID	Central Wavelength (CWL)	Full Width at HalfMaximum (FWHM)	Ratio thermometer
NB 1386–10	1386 ± 5 nm	10 ± 3 nm	Pair 1; Filter 1 (Water absorption)
NB 1912–10	1912 ± 5 nm	10 ± 3 nm	Pair 1; Filter 2 (Water absorption)
NB 1640–25	1640 ± 10 nm	25 ± 10 nm	Pair 2; Filter 1 (Atmosphere window)
NB 2090–25	2090 ± 10 nm	25 ± 10 nm	Pair 2; Filter 2 (Atmosphere window)

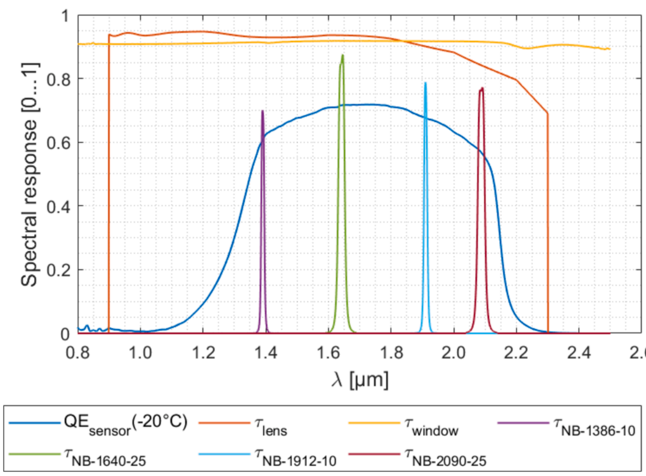

Fig. 5. Spectral response of camera system components.

4.1. Forward problem

In the forward problem, spectral data is known and accessible for simulation (Eq.1–16). On the one hand, the user can define a set of spectra for the tower system. Extraterrestrial solar irradiation (AM0) and atmospheric paths are configured via MODTRAN6 [77,78]. Reference spectra for mirror reflectance and surface emittance are also defined from laboratory measurements. On the other hand, the user can define a camera system spectral response (Fig. 5) and derive corresponding virtual calibration curves (Fig. 6).

Some excerpt visualizations are illustrated here. Fig. 7 displays simulated spectra for the three relevant atmospheric paths shown in Fig. 3. It is worth observing that suitable atmospheric water vapor absorption, around 1.4 μm and 1.9 μm, allows blocking most of solar irradiation on path 1, but also induces significant attenuation on path 3. Fig. 8.a shows the input spectral data for the calculation of ε_{surf}(filter) and $\tau_{atm,path3}$(filter) (Eq.11,12), shown in Fig. 8.b.

Fig. 9 shows a spectral radiometric balance, before applying the camera spectral response (Eq.8). This figure highlights the magnitude of each signal contribution, i.e. terms A, B and C (Eq.3–5). While atmospheric thermal emission (Term C) remain negligible, near solar blindness conditions are rarely met in the SWIR spectral range, except for water absorption bands around 1.4 and 1.9 μm. Fig. 10 shows the same radiometric balance, applying the camera spectral response for each NB filter (Eq.8). This visualization allows determining if the measured signal, i.e. the emitted surface thermal radiation (term A) is dominant over the reflected concentrated solar irradiation (Term B), considered as noise.

4.2. Inverse problem

In the inverse problem, spectral data is no longer accessible, but embedded in the reference forward problem. The aim of the inverse problem is to estimate T_{surf} and $\varepsilon_{surf,band}$, having access to:

i) Calibration functions for each NB filter and the ratio thermometer (Eq.18,19).
ii) Measured signal ratio SR from the forward problem
iii) Model-based $\tau_{atm,path3}$(filter) and $NGCF_{atm}$ from the forward problem

Table 3
Sakuma Hattori fit coefficients for virtual blackbody calibration (Eq.18).

Filter ID	A_1 [W.m^{-2}]	A_2 [K^{-1}]	R^2
NB 1386–10	2.9393 1e5	1.0344 1e4	100 %
NB 1640–25	3.9924 1e5	8.7614 1e3	100 %
NB 1912–10	8.0316 1e4	7.5312 1e3	100 %
NB 2090–25	8.3629 1e4	6.8913 1e3	100 %

Table 4
Fit coefficients for virtual greybody calibration (Eq.19).

Ratio thermometer	Filter 1	Filter 2	B_1 [K^{-1}]	B_2 (intercept)	R^2
Pair 1	NB1386-10	NB1912-10	2.8113 1e3	−1.2946	100 %
Pair 2	NB1640-25	NB2090-25	1.8673 1e3	−1.5591	100 %

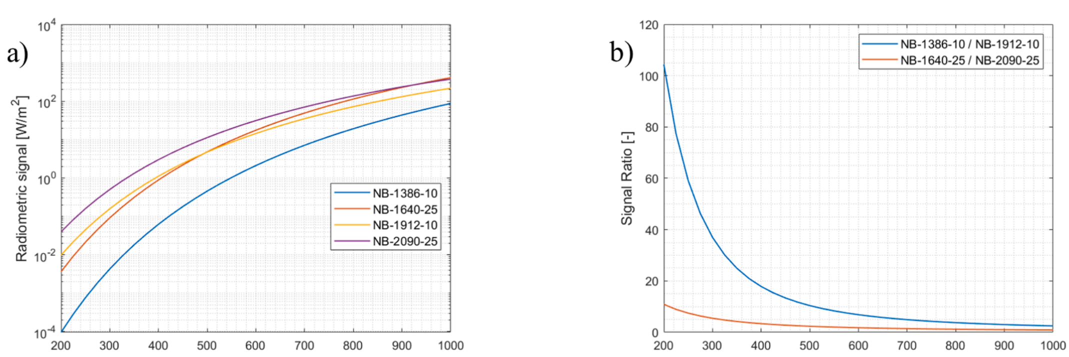

Fig. 6. Camera system response. a) Virtual blackbody calibration for each NB filter [200–1000]°C. b) Virtual greybody calibration for each ratio thermometer [200–1000]°C.

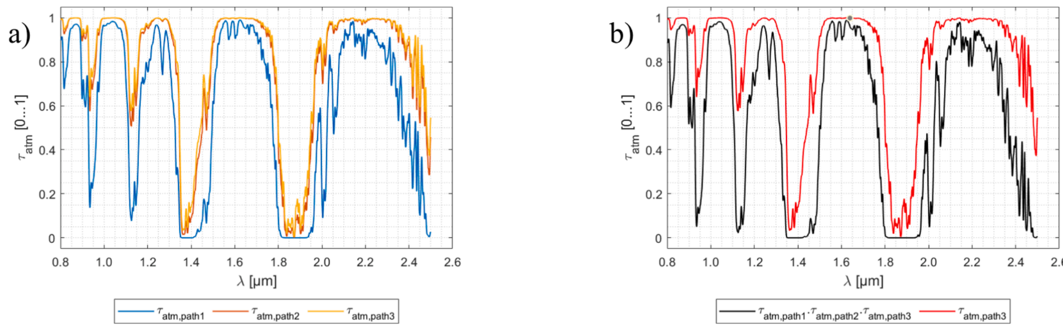

Fig. 7. Spectral simulation of atmospheric paths. Simulation parameters: SZA: 60°(AM2), d_2: 500 m, d_3: 350 m, P_{atm}: 960 mbar, T_{amb}: 30 °C, RH: 30 %. a) Atmospheric transmittance τ_{atm}, for each path. b) Atmospheric transmittance; path product and path 3.

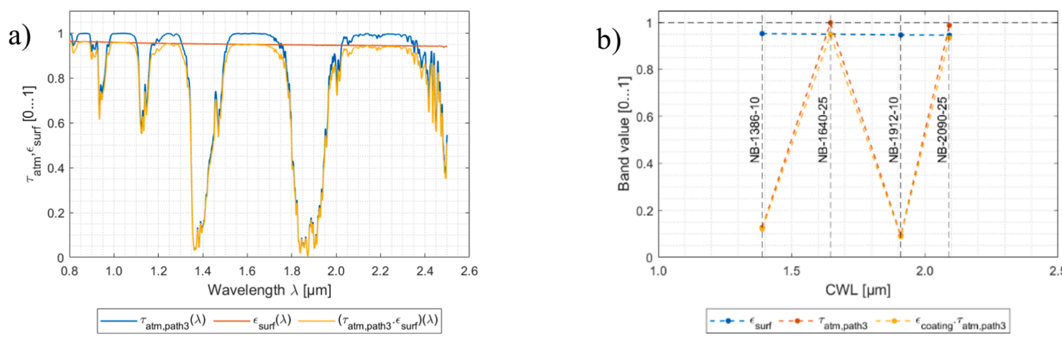

Fig. 8. Surface emittance and atmospheric transmittance. Simulation parameters: Pyromark 2500, SZA: 60° (AM2), d_2: 500 m, d_3: 350 m, P_{atm}: 960 mbar, T_{amb}: 30 °C, RH: 30 %. a) Surface emittance $\varepsilon_{surf}(\lambda)$ for Pyromark 2500 and atmospheric transmittance for path 3 $\tau_{atm,path3}(\lambda)$. b) Surface band emittance ε_{surf}(filter) and atmospheric band transmittance $\tau_{atm,path3}$(filter) for each NB filter.

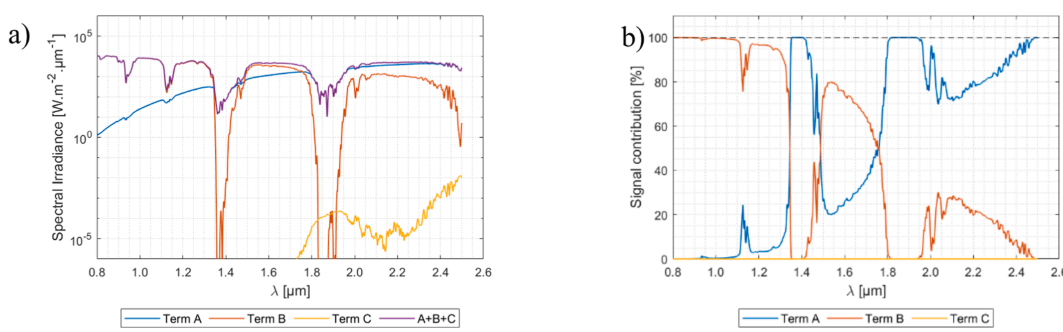

Fig. 9. Spectral radiometric balance. Simulation parameters: Pyromark 2500, T_{surf}: 600 °C, C_x: 300, SZA: 60° (AM2), d_2: 500 m, d_3: 350 m, P_{atm}: 960 mbar, T_{amb}: 30 °C, RH: 30 %. a) Absolute values [W.m^{-2}.μm^{-1}]. b) Relative values [%].

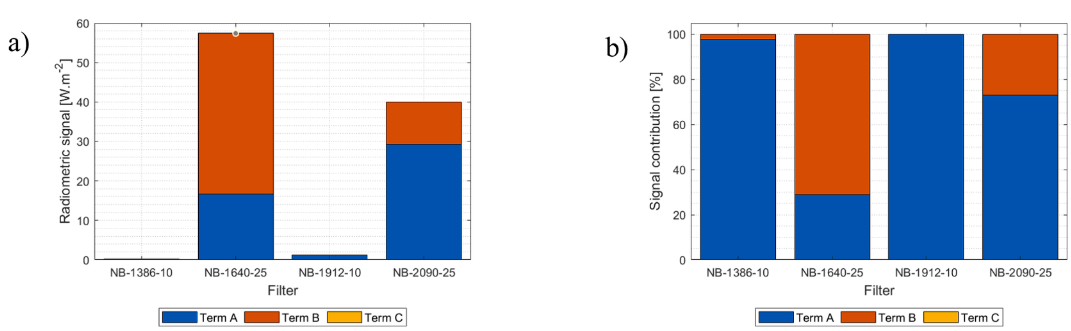

Fig. 10. Band radiometric balance. Simulation parameters: Pyromark 2500, T_{surf}: 600 °C, C_x: 300, SZA: 60° (AM2), d_2: 500 m, d_3: 350 m, P_{atm}: 960 mbar, T_{amb}: 30 °C, RH: 30 %). a) Absolute values [W.m^{-2}]. b) Relative values [%].

Two assumptions are made a priori in order to solve the inverse problem:

- Solar blindness conditions are met, i.e. (Term $B \ll$ Term A)
- The receiver surface behaves as a greybody (ε_{surf}(filter 1) $\sim$ ε_{surf}(filter 2))

Estimated values for T_{surf} and $\varepsilon_{surf,band}$ are then compared to the reference values defined within the reference forward problem to evaluate the accuracy of ratio thermometers. It is worth observing that temperature and emissivity errors are negatively correlated. If the estimated temperature is over-estimated, the estimated band emittance is underestimated and vice versa.

4.3. Batch simulation setup

Simulation parameters are listed in Table 5. The virtual tower power plant is located in Tabernas, Spain. The receiver height is set to 235 m. The equivalent heliostat is positioned at a slant range of 0.5 km. Atmospheric transmittance spectra are generated for the three defined paths using MODTRAN6, defining three meteorological parameters at ground height: P_{atm}, T_{amb}, RH, assuming a Mid-Latitude Summer (MLS) profile for altitude scaling [85]. The default CO_2 concentration is set at 400 ppm. Clear sky conditions are assumed and aerosol scattering is assumed negligible in first approximation for SWIR calculations.

A full factorial design of experiments (DOE) is defined on the one hand for the atmosphere water vapor {P_{atm};T_{amb};RH}, converted into a synthetic variable AH [g/m^3]. This DOE is combined with another full factorial DOE modelling variable operating conditions {T_{surf}; C_x; SZA}. The camera slant range d_3 is also allowed to vary, with a default value set at 350 m.

The aim of this simulation is to analyze the sensitivity of the two SWIR ratio thermometers defined in Section 3.3. The first SWIR ratio thermometer is known to be sensitive to atmospheric water vapor absorption. Suitable atmospheric and operating conditions have to be identified for which the measurement process can be considered nearly solar blind, i.e. for a relative temperature error $\Delta T/T$ less than 2 %, expressing the reference temperature in Kelvins. Once these conditions are identified, ratio temperature measurements can be performed, applying the atmospheric compensation factor $NGCF_{atm}$. Finally, the correlation between the relative temperature error $\Delta T/T$ and the band emittance error $\Delta\varepsilon$ can be characterized. The second SWIR ratio thermometer is insensitive to atmospheric water vapor, solar blind conditions are assumed at dusk, when heliostats are defocused ($C_x = 0$) and the receiver is cooling down before molten salts drainage ($T_{surf} > 250$ °C).

Table 5
Inventory of simulation parameters.

Parameter	Symbol	Category	Units	Value range
Latitude	LAT	Site	[°]	37.0976° North
Longitude	LON	Site	[°]	2.35818° West
Ground height	H_0	Site	m.a.s.l	500 m
Receiver height	H	CRS/ configuration	[km]	235 m
Surface temperature	T_{surf}	CRS/ configuration	[°C]	{200:50:800} °C
Concentration factor	C_x	CRS/ configuration	[-]	{0:100:1000}
Receiver surface	–	CRS/ configuration	–	Pyromark 2500 or H230 oxide
Solar Zenith Angle	SZA	Atmosphere/ Path 1	[°]	{0:10:80} °
Slant range (path 2)	d_2	Atmosphere/ Path 2	[km]	0.5 km (Equivalent heliostat)
Slant range (path 3)	d_3	Atmosphere/ Path 3	[km]	{0.3:0.05:1} km
Atmospheric pressure	$P_{atm}(H_0)$	Atmosphere	[mbar]	960 mbar
Ambient temperature	$T_{amb}(H_0)$	Atmosphere	[°C]	{10:10:40} °C
Relative humidity	RH(H_0)	Atmosphere	[%]	{10:10:90} %
Atmospheric profile	–	Atmosphere	[-]	Mid Latitude Summer (MLS)

5. Results and discussion

5.1. First SWIR ratio thermometer

The first SWIR ratio thermometer (Table 2, Pair 1) combines two NB filters, i.e. NB1386-10 and NB1912-10, which are centered on atmospheric water absorption bands. This SWIR ratio thermometer is thus expected to be sensitive to humidity on the one hand and the atmospheric path length (Fig. 7) on the other hand. Atmospheric water vapor here plays a role in blocking solar irradiation on Path 1 to achieve near solar blindness, while it also attenuates the thermal radiation emitted by the receiver surface on Path 3 (Fig. 3).

Fig. 11 shows the optical depth on path 1 (OD_{path1}) for these two NB filters as a function of AH and SZA. For each NB filter, $\tau_{atm,path1}$(filter) is calculated according to (Eq.21). OD is here defined as the decimal logarithm of $\tau_{atm,path1}$(filter) (Eq.21). An OD value of -3 thus corresponds to an atmospheric transmittance of 0.1 %. To achieve solar blindness, OD_{path1} should thus be minimized.

$$\tau_{atm,path1}(\text{filter}) = \frac{\int_{\lambda_{start}}^{\lambda_{stop}} \tau_{atm,path1}(\lambda, d_1, \text{atm}).E_{sun}(\lambda, \text{AM0}).\text{SRF}_{cam}(\lambda, T_{cam}).d\lambda}{\int_{\lambda_{start}}^{\lambda_{stop}} E_{sun}(\lambda, \text{AM0}).\text{SRF}_{cam}(\lambda, T_{cam}).d\lambda} \tag{20}$$

$$OD_{path1}(\text{filter}) = \log(\tau_{atm,path1}(\text{filter})) \tag{21}$$

For both NB filters, OD_{path1} decreases as AH and SZA increase. A lower OD_{path1} value is observed for the NB1912-10 filter (Fig. 11.b) in comparison to the NB1386-10 filter (Fig. 11.a). This latter NB filter is thus more sensitive to reflected concentrated solar irradiation. The corresponding atmospheric water absorption band around 1.4 µm is narrower in comparison to the next band around 1.9 µm, although both absorption bands broaden as AH and SZA increase.

Fig. 12 shows the atmospheric transmittance on path 3 ($\tau_{atm,path3}$) for both NB filters as a function of AH and slant range d_3. For both NB filters, $\tau_{atm,path3}$ decreases as AH and d_3 increase. A significant attenuation is observed, the maximum transmittance is about 30 % for a dry atmosphere and a slant range d_3 of 300 m. This is the minimal applicable slant range for a typical receiver height of 235 m.

Fig. 13 shows the expected relative error $\Delta T/T$ (%) for the first SWIR ratio thermometer as a function of T_{surf}, C_x, SZA and AH. The reference surface is Pyromark 2500 and slant range d_3 is set at 350 m. Four sections of the simulated hypercube are shown, i.e. for low and high absolute humidity at ground level (AH: 6 …15 g/m^3) and for low and high concentration factor (C_x: 300…1000). The relative error $\Delta T/T$ should be less than 2 % for an accurate surface temperature measurement. This criterion allows defining a minimal temperature threshold. Fig. 13 shows that this temperature threshold is dynamic. If AH $\sim$ 6 g/m^3, the minimum temperature threshold is respectively 530 °C for $C_x = 300$ and 620 °C for $C_x = 1000$. If AH $\sim$ 15 g/m^3, the minimum temperature threshold is 590 °C for $C_x = 300$ and 690 °C for $C_x = 1000$. These temperature thresholds overlap or even exceed the maximum T_{surf} value allowed for molten salt receivers, i.e. $\sim$ 600 °C. These thresholds slightly relax by at least 10 K at higher SZA above 45° (winter or sunrise/sunset). This limits significantly the applicability of this first SWIR ratio thermometer for remote opto-thermal characterization.

Fig. 14 shows the correlation between the absolute band emittance error $\Delta\varepsilon$ and the relative temperature error $\Delta T/T$ for the first SWIR ratio thermometer, applying as threshold $\Delta T/T < 2$ %. A linear negative correlation is observed between $\Delta\varepsilon$ and $\Delta T/T$ for Pyromark 2500

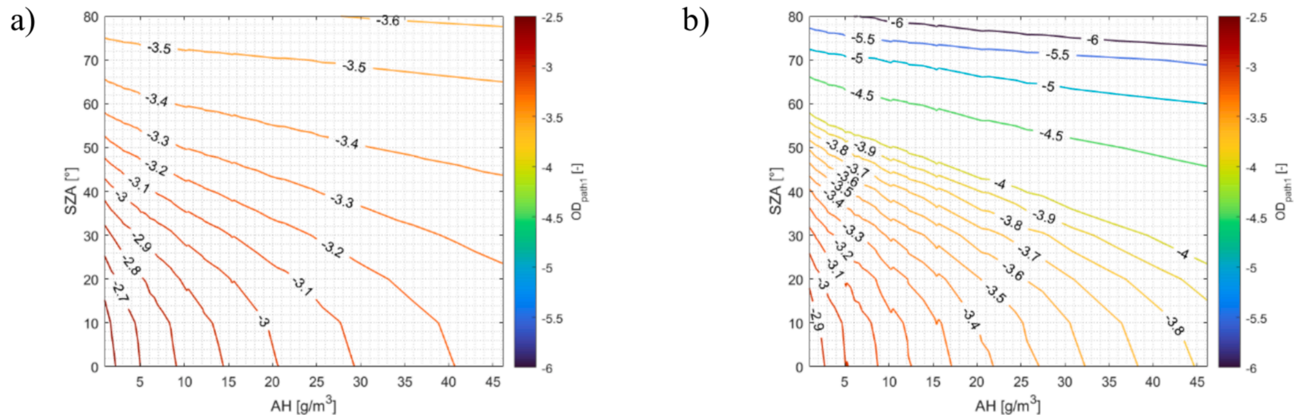

Fig. 11. Contour plot of OD_{path1} as a function of AH and SZA. a) NB1386-10, b) NB1912-10.

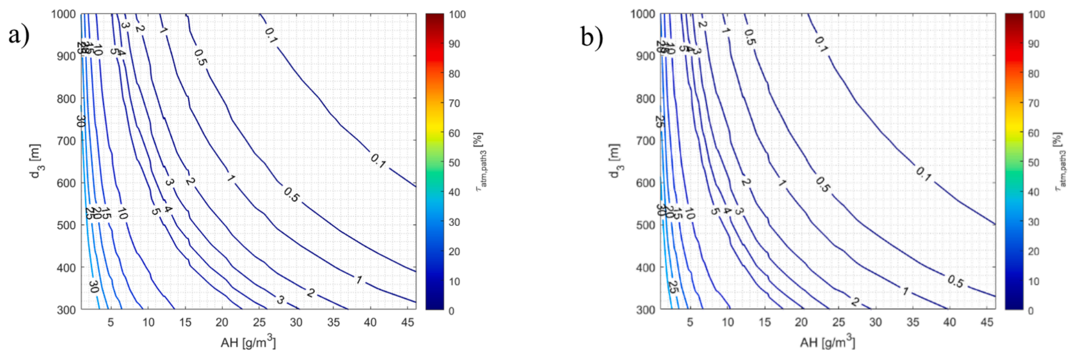

Fig. 12. Contour plot of $\tau_{atm,path3}$ as a function of AH and d_3. a) NB1386-10, b) NB1912-10.

(Fig. 14a) and oxidized H230 (Fig. 14b). Reference ε_{surf}(filter) values for both surfaces are given in Table 6. The grey hypothesis is confirmed for both surfaces, although the ratio of band emittance is slightly lower for oxidized H230. For Pyromark 2500, the correlation slope coefficient is estimated at -6.3p.p. $\Delta\varepsilon$ for a 1 % variation of $\Delta T/T$ (Fig. 14a). For oxidized H230, the correlation slope coefficient is estimated at -5.7p.p. $\Delta\varepsilon$ / 1 % $\Delta T/T$ (Fig. 14b).

5.2. Second SWIR ratio thermometer

The second SWIR ratio thermometer (Table 2, Pair 2) combines two NB filters, i.e. NB1640-25 and NB2090-25, which are centered on atmospheric windows. This SWIR ratio thermometer is not suitable for on-sun temperature measurements. This configuration is thus analysed for off-sun ($C_x = 0$) temperature measurements, with $T_{surf} > 250$ °C (molten salts freezing point).

Fig. 15 shows the atmospheric transmittance on path 3 ($\tau_{atm,path3}$) for both NB filters as a function of AH and slant range d_3. The filter NB1640-25 is barely affected by AH and d_3 parameters (Fig. 15a), $\tau_{atm,path3}$(filter) values remain above 99 %. For the filter NB2090-25, a minor dependence is observed (Fig. 15b), although $\tau_{atm,path3}$(filter) values remain above 90 %. Both NB filters are thus suited for remote opto-thermal characterization.

Fig. 16 shows the expected relative error $\Delta T/T$ for the second SWIR ratio thermometer as a function of T_{surf} and AH for both reference surfaces. The concentration factor C_x is set at 0 and the slant range d_3 is set at 350 m. One can first observe that $\Delta T/T$ is independent of AH and increase linearly with T_{surf}. Furthermore, the expected value for $\Delta T/T$ is low for both surfaces: for Pyromark 2500, $\Delta T/T$ is bounded between 0.12 % at 250 °C and 0.26 % at 800 °C. For oxidized H230, $\Delta T/T$ is bounded between 0.16 % at 250 °C and 0.34 % at 800 °C.

If the central receiver cannot be heated to an arbitrary temperature T_{surf} above 300 °C with a suitable heat tracing system, this SWIR ratio thermometer could only be used in practice for low receiver surface temperature levels. The central receiver must be maintained isothermal, above the molten salt freezing temperature, when the heliostat field is defocused ($C_x = 0$). This would correspond to the daily cool-down operation phase before molten salt drainage, when the calibration of the reference LWIR thermographic system is typically performed.

Fig. 17 shows the correlation between the absolute emissivity error $\Delta\varepsilon$ and the relative temperature error $\Delta T/T$ for the second SWIR ratio thermometer. A negative correlation is observed between $\Delta\varepsilon$ and $\Delta T/T$ for Pyromark 2500 (Fig. 17.a) and oxidized H230 (Fig. 17b). Reference ε_{surf}(filter) values for both surfaces are given in Table 7. The grey hypothesis is confirmed for both surfaces. The estimated band emittance is systematically underestimated. For Pyromark 2500, the absolute value of $\Delta\varepsilon$ does not exceed 2p.p., while its maximum value is about 2.5p.p. for oxidized H230. The second SWIR ratio thermometer allows discriminating both surfaces.

6. Conclusion and outlook

In this paper, a new measurement principle has been introduced and analysed for the remote opto-thermal characterization of central external receivers in solar tower power plants. The new measurement principle relies on passive shortwave infrared (SWIR) ratio thermography. It allows a simultaneous retrieval of surface temperature and band emittance for grey surfaces such as black coatings and oxidized metals. The atmosphere does not behave a priori as a greybody. A model-based estimation of band atmospheric transmittance has been introduced to correct this hypothesis, using meteorological parameters available at ground level, i.e. ambient temperature T_{amb}, relative humidity RH and atmospheric pressure P_{atm}.

A MATLAB software tool has been developed and coupled to

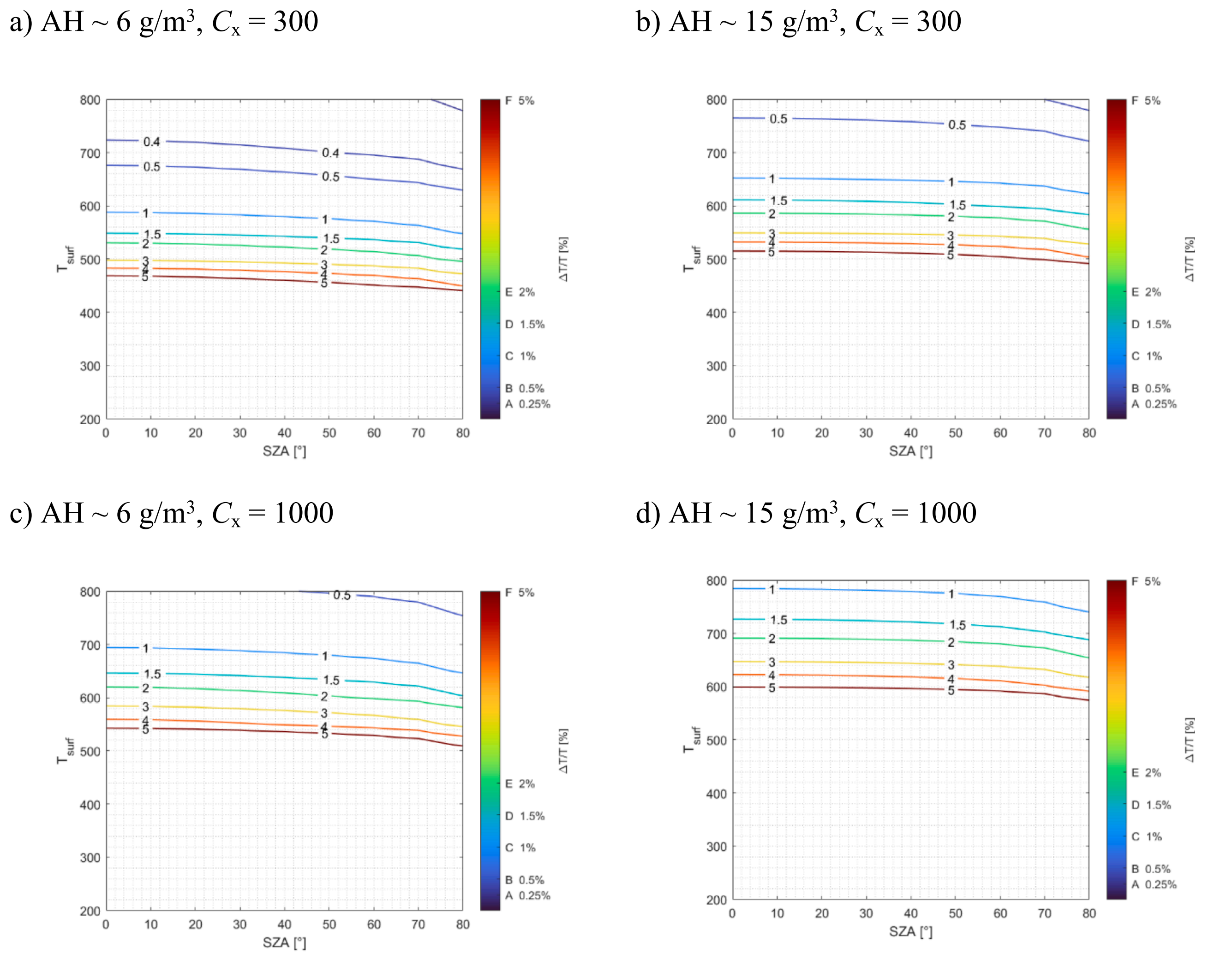

Fig. 13. Analysis of relative temperature error $\Delta T/T$ as a function of SZA, AH, T_{surf} and C_x. Boundary conditions: $d_3 = 350$ m, Pyromark 2500. $P_{atm} = 960$ mbar, $T_{amb} = 30$ °C, RH: (20…50) %.

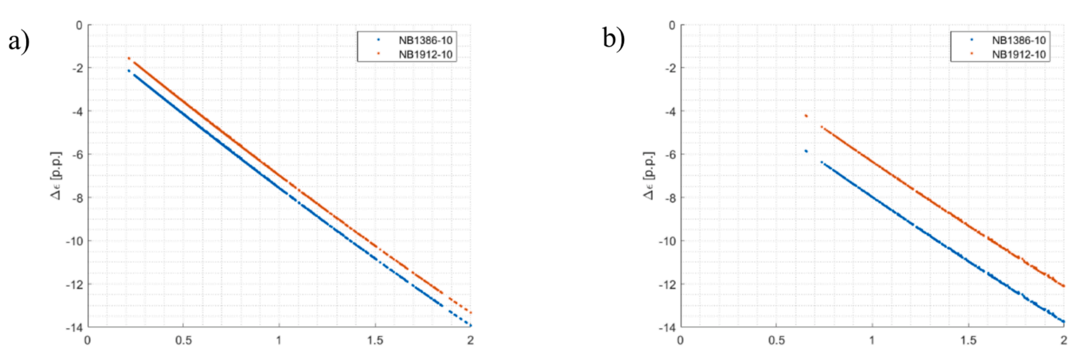

Fig. 14. Correlation of $\Delta\varepsilon$ and $\Delta T/T$ for the first SWIR ratio thermometer. Boundary conditions: $\Delta T/T < 2$ %; $d_3 = 350$ m. a) Pyromark 2500. b) Oxidized H230.

Table 6
First SWIR ratio thermometer. Reference band emittance values ε_{surf}(filter) for Pyromark 2500 and oxidized H230.

ε_{surf}(filter)	Filter 1: NB1386-10	Filter 2: NB1912-10	Grey hypothesis
Pyromark 2500	95.3 %	94.7 %	99.4 %
Oxidized H230	87.8 %	86.2 %	98.2 %
Deviation	7.5p.p.	8.5p.p.	–

MODTRAN6 radiative transfer code, for the spectral simulation of radiometric chains relevant in Concentrating Solar Power. The accuracy and sensitivity of two SWIR ratio thermometers have been analysed using spectral simulations. Relevant parameters combine atmospheric conditions, in particular absolute humidity AH and Solar Zenith Angle (SZA) and operating conditions, i.e. surface temperature T_{surf} and concentration factor C_x. The first SWIR ratio thermometer combines two narrow bandpass (NB) filters centered on two water vapor atmospheric absorption bands, respectively located at 1.4 μm and 1.9 μm. The second

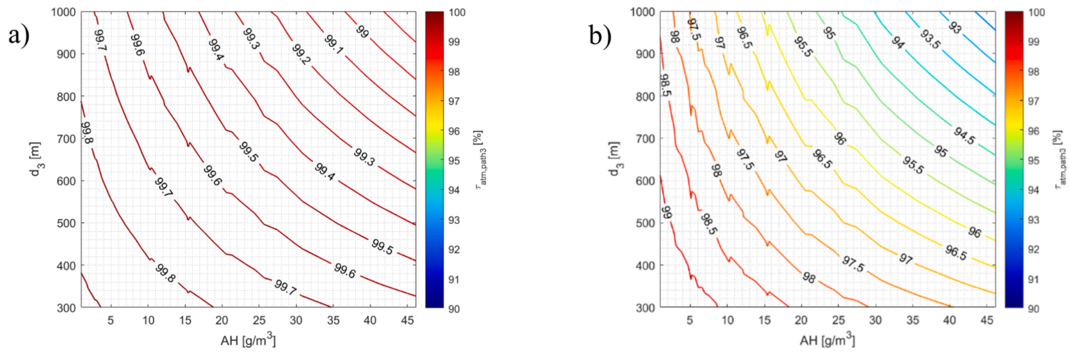

Fig. 15. Contour plot of $\tau_{\mathrm{atm,path3}}$ as a function of AH and d_3. a) NB1640-25, b) NB2090-25.

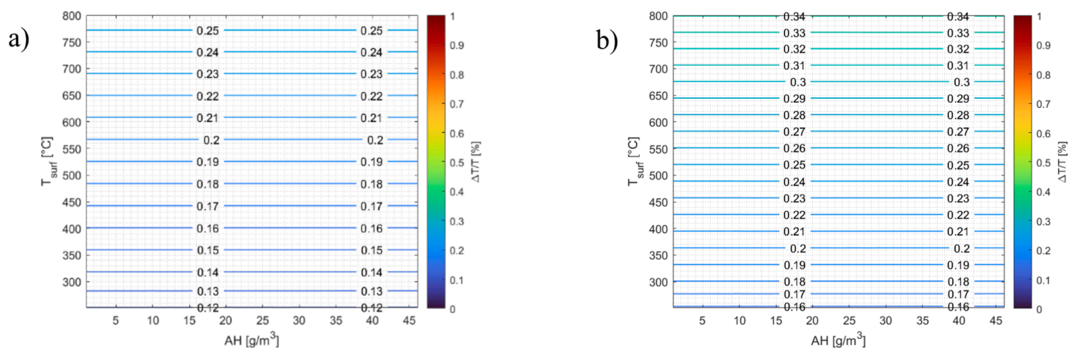

Fig. 16. Analysis of relative temperature error $\Delta T/T$ as a function of T_{surf}. Boundary conditions: $d_3 = 350$ m, $C_{\mathrm{x}} = 0$. a) Pyromark 2500. b) oxidized H230.

SWIR ratio thermometer combines two NB filters centered on atmospheric windows, respectively located at 1.64 μm and 2.09 μm.

The first SWIR ratio thermometer (1.4/1.9 μm) is particularly sensitive to atmospheric water vapor, which filters extraterrestrial solar radiation on the one hand but also attenuates thermal radiation emitted by the receiver surface on the other hand, in particular for a typical receiver height above 200 m. Under realistic AH levels, this ratio thermometer can be considered nearly solar blind, but only for temperature above 550 °C. The temperature threshold for which the relative temperature error $\Delta T/T$ is less than 2 % varies with the absolute humidity AH estimated at ground level, the solar zenith angle SZA and the concentration factor C_{x}. This SWIR ratio thermometer, originally designed for remote opto-thermal characterization during power plant operation, has probably a limited applicability, especially for a receiver height above 200 m.

The second SWIR ratio thermometer (1.64/2.09 μm) is not sensitive to atmospheric water vapor, however it cannot operate during daily power plant operation. It could remotely characterise the receiver surface temperature T_{surf} and surface band emittance $\varepsilon_{\mathrm{surf,band}}$ with a good accuracy when the heliostat field is defocused ($C_{\mathrm{x}} = 0$) and the receiver surface is maintained isothermal ($T_{\mathrm{surf}} \sim 300$ °C) before molten salt drainage. The relative temperature error $\Delta T/T$ is lower than 0.5 % and the band emittance error $\Delta\varepsilon$ is less than 2.5p.p., according to spectral simulations for Pyromark 2500 and oxidized Haynes 230.

This operation phase is also often used in commercial power plants for the calibration of Longwave Infrared (LWIR) cameras. The second SWIR ratio thermometer could therefore offer an alternative method to support the LWIR system during calibration and map remotely the receiver band emittance.

A prototype SWIR multispectral camera, including both ratio thermometer configurations described above, has been assembled and tested at Plataforma Solar de Almería, Spain. The experimental validation of the measurement principle under laboratory conditions is currently ongoing and the camera system is being fine-tuned for future field measurements in Central Receiver Systems.

Future simulation work may investigate the sensitivity of both SWIR ratio thermometers with respect to aerosols or water vapor atmospheric profiles. The software tool for spectral simulations is also capable to

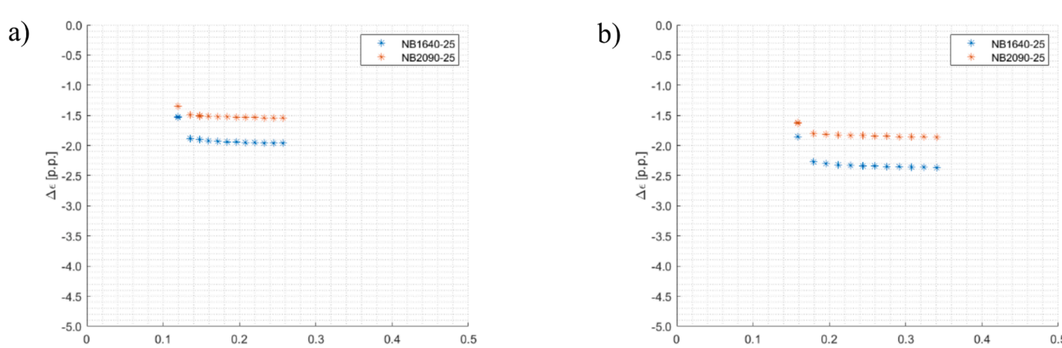

Fig. 17. Correlation of $\Delta\varepsilon$ and $\Delta T/T$ for the second SWIR ratio thermometer. Boundary conditions: $C_{\mathrm{x}} = 0$, $d_3 = 350$ m. a) Pyromark 2500. b) Oxidized H230.

Table 7
Second SWIR ratio thermometer. Reference band emittance values ε_{surf}(filter) for Pyromark 2500 and oxidized H230.

ε_{surf}(filter)	Filter 1: NB1640-25	Filter 2: NB2090-25	Grey hypothesis
Pyromark 2500	95.0 %	94.6 %	99.6 %
Oxidized H230	86.7 %	86.2 %	99.4 %
Deviation	8.3p.p.	8.7p.p.	–

simulate other spectral ranges, i.e. visible wavelengths (0.4–0.8 μm) for flux measurement systems, as well as midwave and infrared wavelengths (MWIR: 2.5–5.5 μm, LWIR: 8–14 μm) relevant for other thermographic camera configurations.

CRediT authorship contribution statement

Simon Caron: Conceptualization, Formal analysis, Investigation, Methodology, Software, Validation, Visualization, Writing – original draft, Writing – review & editing. **Romain Larue:** Formal analysis, Investigation, Software, Writing – original draft, Writing – review & editing. **Andreas Kämpgen:** Methodology, Writing – review & editing, Conceptualization. **Florian Sutter:** Conceptualization, Methodology, Writing – review & editing. **Marc Röger:** Conceptualization, Methodology, Project administration, Supervision, Writing – review & editing, Funding acquisition. **Michael Nieslony:** Writing – review & editing. **Francisco Manzano-Agugliaro:** Supervision, Writing – review & editing.

Declaration of competing interest

The authors declare the following financial interests/personal relationships which may be considered as potential competing interests: The main author declares a potential competing interest related to intellectual property rights that may influence the work reported in this paper. The authors Simon Caron, Andreas Kämpgen, Florian Sutter and Marc Röger have a joint patent application #DE 10 2023 106 003 A1, submitted on 10.03.2023 and registered on 14.09.2023, issued to the German Aerospace Center (DLR) and CSP Services. This patent application is directly related to the measurement principle presented in this work.

Acknowledgments

This work has received funding from the European Union's Horizon 2020 Research and Innovation Program under grant agreement n°823802 (SFERA-III), n°838311 (LEIA, Solar-Era.Net) and (TubeMon, Solar-Era.Net). The project TubeMon was financially supported by the Federal Republic of Germany (BMWK, Federal Ministry for Economic Affairs and Climate Protection) on the basis of a resolution of the German Bundestag (FKZ 03EE5008) and the Kingdom of Spain (Ministry of Science, Innovation and Universities), through the Centre for the Development of Technology and Innovation (CDTI) (SERA-20201001). The initial contributions of Luca Ressel (Stuttgart University) and Albin Englin (Linköping University) in the development of the spectral simulation software tool are also acknowledged.

References

[1] M. Perez, R. Perez, Update 2022 – A fundamental look at supply side energy reserves for the planet, *Sol. Energy Adv.* 2 (2022) 100014, https://doi.org/10.1016/j.seja.2022.100014.
[2] MIT Energy Initiative, The Future of Solar Energy (2015), https://energy.mit.edu/wp-content/uploads/2015/05/MITEI-The-Future-of-Solar-Energy.pdf, Last accessed 01/12/23.
[3] IRENA, Solar Energy, https://www.irena.org/Energy-Transition/Technology/Solar-energy, Last accessed 01/12/23.
[4] PV magazine, World has installed 1TW of solar capacity, https://www.pv-magazine.com/2022/03/15/humans-have-installed-1-terawatt-of-solar-capacity/, Last accessed 01/12/23.
[5] IEA SolarPACES, CSP projects around the world, https://www.solarpaces.org/worldwide-csp/csp-projects-around-the-world/, Last accessed 01/12/23.
[6] IEA SolarPACES, https://www.solarpaces.org/china-now-has-30-csp-projects-with-thermal-energy-storage-underway/, Last accessed 01/12/23.
[7] German Aerospace Center (DLR) Institute of Solar Research, Solar thermal power plants: heat, electricity and fuels from concentrated solar power, (2021), https://www.dlr.de/sf/en/PortalData/73/Resources/dokumente/publikationen_medien/dlr_und_sf/Study_Solar_thermal_power_plants_DLR_2021-05.pdf. Last accessed 30/11/2023.
[8] DCSP, German Association for Concentrated Solar Power, Solar Power around the Clock, (2021), EN%20211116_DCSP_Kurzstudie_online_EN.pdf (website-editor.net), Last accessed 30/11/2023.
[9] Solar Payback, Solar Heat for Industry, (2017), https://www.solar-payback.com/download/solar-heat-for-industry-april-2017/, Last accessed 30/11/2023.
[10] R. Pitz-Paal, J. Krüger, J. Hinsch, A. Lokurlu, M. Scheuerer, M. Schlecht, M. Schmitz, G. Schreiber, Decarbonizing the German industrial thermal energy use with solar, hydrogen, and other options–Recommendations for the world, *Sol. Compass* 3–4 (2022) 100029, https://doi.org/10.1016/j.solcom.2022.100029.
[11] R. Bader, W. Lipiński, Advances in Concentrating Solar Thermal Research and Technology, Woodhead Publishing, 2017, pp. 403–459, https://doi.org/10.1016/B978-0-08-100516-3.00018-6.
[12] W. Lipiński, Solar Thermochemistry, First Edition, Academic Press, 2021.
[13] W.-D. Steinmann, Concentrating Solar Power Technology, Second Edition, Woodhead Publishing, 2020, pp. 399–440, https://doi.org/10.1016/B978-0-12-819970-1.00008-6.
[14] A. Fernandez-Garcia, E. Zarza, L. Valenzuela, M. Perez, Parabolic-trough solar collectors and their applications, *Renew. Sustain. Energy Rev.* 14 (2010) 1695–1721, https://doi.org/10.1016/j.rser.2010.03.012.
[15] G. Zhu, T. Wendelin, M.J. Wagner, C. Kutscher, History, current state, and future of linear Fresnel concentrating solar collectors, *Sol. Energy* 103 (2014) 639–652, https://doi.org/10.1016/j.solener.2013.05.021.
[16] C.K. Ho, Advances in central receivers for concentrating solar applications, *Sol. Energy* 152 (2017) 38–56, https://doi.org/10.1016/j.solener.2017.03.048.
[17] P. Gauche, J. Rudman, M. Mabaso, W.A. Landman, T.W. von Backström, A. C. Brent, System value and progress of CSP, *Sol. Energy* 152 (2017) 106–139, https://doi.org/10.1016/j.solener.2017.03.072.
[18] M. Zheng, J. Zapata, C.-A. Asselineau, J. Coventry, J. Pye, Analysis of tubular receivers for concentrating solar tower systems with a range of working fluids, in exergy-optimised flow-path configurations, *Sol. Energy* 211 (2020) 999–1016, https://doi.org/10.1016/j.solener.2020.09.037.
[19] C.-A. Asselineau, J. Pye, J. Coventry, Exploring efficiency limits for molten-salt and sodium external cylindrical receivers for third-generation concentrating solar power, *Sol. Energy* 240 (2022) 354–375, https://doi.org/10.1016/j.solener.2022.05.001.
[20] C.K. Ho, A. Roderick Mahoney, A. Ambrosini, M. Bencomo, A. Hall, T.N. Lambert, Characterization of Pyromark 2500 paint for high-temperature solar receivers, *J. Sol. Energy Eng.* 136 (1) (2014) 014502, https://doi.org/10.1115/1.4024031.
[21] J. Coventry, P. Burge, Optical properties of Pyromark 2500 coatings of variable thicknesses on a range of materials for concentrating solar thermal applications, *AIP Conf. Proc.* 2017 (1850) 030012, https://doi.org/10.1063/1.4984355.
[22] A. Ambrosini, A. Boubault, C.K. Ho, L. Banh, J.R. Lewis, Influence of application parameters on stability of Pyromark® 2500 receiver coatings, *AIP Conf. Proc.* 2126 (2019) 030002, https://doi.org/10.1063/1.5117514.
[23] R. Harzallah, M. Larnicol, C. Leclercq, A. Herebein, F. Campana, Development of high performances solar absorber coatings, *AIP Conf. Proc.* 2126 (2019) 030026, https://doi.org/10.1063/1.5117538.
[24] L. Noč, E. Šest, G. Kapun, F. Ruiz-Zepeda, Y. Binyamin, F. Merzel, I. Jerman, High-solar-absorptance CSP coating characterization and reliability testing with isothermal and cyclic loads for service-life prediction, *Energ. Environ. Sci.* 12 (2019) 1679–1694, https://doi.org/10.1039/C8EE03536A.
[25] J.F. Torres, K. Tsuda, Y. Murakami, Y. Guo, S. Hosseini, C.-A. Asselineau, M. Taheri, K. Drewes, A. Tricoli, W. Lipinski, J. Coventry, Highly efficient and durable solar thermal energy harvesting via scalable hierarchical coatings inspired by stony corals, *Energ. Environ. Sci.* 15 (2022) 1893–1906, https://doi.org/10.1039/D1EE03028K.
[26] L. Martínez-Manuel, N.G. González-Canché, L.B. López-Sosa, J.G. Carrillo, W. Wang, C.A. Pineda-Arellano, F. Cervantes, J.J. Alvarado Gil, M.I. Peña-Cruz, A comprehensive analysis of the optical and thermal performance of solar absorber coatings under concentrated flux conditions, *Sol. Energy* 239 (2022) 319–336, https://doi.org/10.1016/j.solener.2022.05.015.
[27] F. Sutter, C. Oskay, M.C. Galetz, T. Diamantino, F. Pedrosa, I. Figueira, S. Glumm, A. Bonk, A. Agüero, S. Rodriguez, T.J. Reche-Navarro, S. Caron, Dynamic corrosion testing of metals in solar salt for concentrated solar power, *Sol. Energy Mater. Sol. Cells* 232 (2021) 111331, https://doi.org/10.1016/j.solmat.2021.111331.
[28] D. Hering, M. Binder, P. Schwarzbözl, R. Schwaiger, R. Pitz-Paal, Monitoring of service life consumption for tubular solar receivers: Review of contemporary thermomechanical and damage modeling approaches, *Sol. Energy* 226 (2021) 427–445, https://doi.org/10.1016/j.solener.2021.08.022.
[29] L.L. Vant-Hull, The Role of "Allowable Flux Density" in the Design and Operation of Molten-Salt Solar Central Receivers, *J. Sol. Energy Eng.* 124 (2) (2002) 165–169, https://doi.org/10.1115/1.1464124.
[30] R. Flesch, C. Frantz, D. Maldonado Quinto, P. Schwarzbözl, Towards an optimal aiming for molten salt power towers, *Sol. Energy* 155 (2017) 1273–1281, https://doi.org/10.1016/j.solener.2017.07.067.

[31] A. Sanchez-Gonzalez, M.R. Rodriguez-Sanchez, D. Santana, Aiming strategy model based on allowable flux densities for molten salt central receivers, *Sol. Energy* 157 (2017) 1130–1144, https://doi.org/10.1016/j.solener.2015.12.055.

[32] M. Röger, P. Herrmann, S. Ulmer, M. Ebert, C. Prahl, F. Göhring, Techniques to Measure Solar Flux Density Distribution on Large-Scale Receivers, *J. Sol. Energy Eng.* 136 (3) (2014) 031013, https://doi.org/10.1115/1.4027261.

[33] W. Lipiński, J.H. Davidson, S. Haussener, J.F. Klausner, A.M. Mehdizadeh, J. Petrasch, A. Steinfeld, L. Venstrom, Review of Heat Transfer Research for Solar Thermochemical Applications, *J. Therm. Sci. Eng. Appl.* 5 (2) (2013) 021005, https://doi.org/10.1115/1.4024088.

[34] J.F. Torres, I. Ellis, J. Coventry, Degradation mechanisms and non-linear thermal cycling effects in a high-temperature light-absorber coating, *Sol. Energy Mater. Sol. Cells* 218 (2020) 110719, https://doi.org/10.1016/j.solmat.2020.110719.

[35] S. Hosseini, J.F. Torres, M. Taheri, A. Tricoli, W. Lipinski, J. Coventry, Long-term thermal stability and failure mechanisms of Pyromark 2500 for high-temperature solar thermal receivers, *Sol. Energy Mater. Sol. Cells* 246 (2022) 111898, https://doi.org/10.1016/j.solmat.2022.111898.

[36] N. Martinez, M. Lopez-Herraiz, A. Rico, C.J. Munez, P. Poza, Influence of different thermal degradation processes on the optical property of Pyromark-2500, *Sol. Energy* 253 (2023) 58–72, https://doi.org/10.1016/j.solener.2023.02.004.

[37] S. Caron, J. Garrido, E. Setien, R. Harzallah, L. Noč, I. Jerman, M. Röger, F. Sutter, Forty shades of black: A benchmark of high temperature sprayable black coatings applied on Haynes 230, *AIP Conf. Proc.* 2303 (2020) 150007, https://doi.org/10.1063/5.0028773.

[38] S. Caron, J. Garrido, J. Ballestrin, F. Sutter, M. Röger, F. Manzano-Agugliaro, A comparative analysis of opto-thermal figures of merit for high temperature solar thermal absorber coatings, 21, *Renewable Sustainable Energy Review* 154 (2022) 111818, https://doi.org/10.1016/j.rser.2021.111818.

[39] S. Caron, L. Herding, Y. Binyamin, M. Baidossi, Y. Vinetsky, A. Morales, C. Hildebrandt, R. Reoyo-Prats, O. Faugeroux, A. Agüero, S. Rodriguez, F. Sutter, M. Röger, F. Manzano-Agugliaro, A laboratory intercomparison of solar absorptance and thermal emittance measurements at room temperature, *Solar Energy Materials and Solar Cells* 238 (2022) 15, 111579. https://doi.org/10.1016/j.solmat.2022.111579.

[40] C.K. Ho, J. Pacheco, Levelized Cost of Coating (LCOC) for selective absorber materials, *Sol. Energy* 108 (2014) 315–321, https://doi.org/10.1016/j.solener.2014.05.017.

[41] A. Boubault, C.K. Ho, A. Hall, T.N. Lambert, A. Ambrosini, Levelized cost of energy (LCOE) metric to characterize solar absorber coatings for the CSP industry, *Renew. Energy* 85 (2016) 472–483, https://doi.org/10.1016/j.renene.2015.06.059.

[42] J. Ballestrín, M.-I. Roldán, Contact sensors for measuring high surface temperature in concentrated solar radiation environments, *Measurement* 109 (2017) 65–73, https://doi.org/10.1016/j.measurement.2017.05.039.

[43] M. Pfänder, D. Hernandez, A. Neumann, E. Lüpfert, W. Lipiński, H.-R. Tschudi, J. Ballestrín, Solar-blind pyrometric temperature measurement under concentrated solar irradiation, *SolarPACES Conference Proceedings* (2006). https://elib.dlr.de/44704/.

[44] J. Mahal, P. Good, G. Ambrosetti, T.A. Cooper, Contactless thermal mapping of high-temperature solar receivers via narrow-band near-infrared thermography, *Sol. Energy* 246 (2022) 331–342.

[45] InfraTec GmbH, https://www.infratec.eu/thermography/industrial-automation/solar-power-tower-check-sptc/, Last accessed 30/11/2023.

[46] Surface Optics Corporation, https://surfaceoptics.com/products/reflectometers-emissometers/410-vis-ir/, Last accessed 30/11/2023.

[47] M. Mehos, H. Price, R. Cable, D. Kearney, B. Kelly, G. Kolb, F. Morse, Concentrating Solar Power Best Practices Study, *NREL Technical report*, NREL/TP-5500-75763 (2020). https://www.nrel.gov/docs/fy20osti/75763.pdf.

[48] G. Naor, G. Goldwine, R. Hayut, O. Bibi, E. Silberstein, O. Chernin, Z. Auman, G. Kroyzer, A. Ziskin, Flux measurement system using IR camera, *SolarPACES 2010 Proceedings*, Perpignan, France, September 21-24, 2010.

[49] A. Eitan, G. Naor, R. Hayut, I. Segev, J. Golbert, S. Pekarsky, A. Zisken, G. Medan, A. Feigelstock, N. Goldberg, G. Kroyzer, Accurate Flux Calculations Using Thermographic IR cameras in Concentrated Solar Power Fields, *Quantitative Infrared Thermography (QIRT) 2014 Conference Proceedings*, http://qirt.org/archives/qirt2014doi/papers/QIRT-2014-220.pdf.

[50] I. González de Arrieta, T. Echaniz, R. Fuente, E. Rubin, R. Chen, J.M. Igartua, M. J. Tello, G.A. López, Infrared emissivity of copper-alloyed spinel black coatings for concentrated solar power systems, *Sol. Energy Mater. Sol. Cells* 200 (2019) 109961, https://doi.org/10.1016/j.solmat.2019.109961.

[51] W. Minkina, D. Klecha, Atmospheric transmission coefficient modelling in the infrared for thermovision measurements, *Journal of Sensors and Sensors Systems* 5 (2016) 17–23, https://doi.org/10.5194/jsss-5-17-2016.

[52] D. Hernandez, G. Olalde, J.M. Gineste, C. Gueymard, Analysis and Experimental Results of Solar-Blind Temperature Measurements in Solar Furnaces, *J. Sol. Energy Eng.* 126 (1) (2004) 645–653, https://doi.org/10.1115/1.1636191.

[53] J. Ballestrin, A. Marzo, I. Cañadas, J. Rodríguez, Testing a solar-blind pyrometer, *Metrologia* 47 (2010) 646, https://doi.org/10.1088/0026-1394/47/6/003.

[54] A. Marzo, J. Ballestrin, J. Barbero, I. Cañadas, J. Rodríguez, Solar blind pyrometry not relying on atmospheric absorption bands, *Solar Energy* 107 (2014) 415–422, https://doi.org/10.1016/j.solener.2014.04.031.

[55] M. Pfänder, E. Lüpfert, P. Heller, Pyrometric Temperature Measurements on Solar Thermal High Temperature Receivers, *J. Sol. Energy Eng.* 128 (3) (2006) 285–292, https://doi.org/10.1115/1.2210499.

[56] M. Pfänder, E. Lüpfert, P. Pistor, Infrared temperature measurements on solar trough absorber tubes, *Sol. Energy* 81 (5) (2007) 629–635, https://doi.org/10.1016/j.solener.2006.08.016.

[57] M. Musto, G. Rotondo, M. De Cesare, A. Del Vecchio, L. Savino, F. De Filippis, Error analysis on measurement temperature by means dual-color thermography technique, *Measurement* 90 (2016) 265–277, https://doi.org/10.1016/j.measurement.2016.04.024.

[58] L. Savino, M. De Cesare, M. Musto, G. Rotondo, F. De Filippis, A. Del Vecchio, F. Russo, Free emissivity temperature investigations by dual color applied physics methodology in the mid- and long-infrared ranges, *Int. J. Therm. Sci.* 117 (2017) 328–341, https://doi.org/10.1016/j.ijthermalsci.2017.03.028.

[59] F. Di Carolo, L. Savino, D. Palumbo, A. Del Vecchio, U. Galietti, M. De Cesare, Standard thermography vs free emissivity dual color novel CIRA physics technique in the near-mid IR ranges: Studies for different emissivity class materials from low to high temperatures typical of aerospace re-entry, *Int. J. Therm. Sci.* 147 (2020) 106123, https://doi.org/10.1016/j.ijthermalsci.2019.106123.

[60] A. Hijazi, S. Sachidanandan, R. Singh, V. Madhavan, A calibrated dual-wavelength infrared thermometry approach with non-grey body compensation for machining temperature measurements, *Meas. Sci. Technol.* 22 (2011) 025106, https://doi.org/10.1088/0957-0233/22/2/025106.

[61] A. Araujo, Multi-spectral pyrometry – a review, *Meas. Sci. Technol.* 28 (2017) 082002, https://doi.org/10.1088/1361-6501/aa7b4b.

[62] J.-C. Krapez, Measurements without contact in heat transfer: multiwavelength radiation thermometry. Principle, implementation and pitfalls, *Metti 7 Advanced School: Thermal Measurements and Inverse Techniques*, (2019) Porquerolles, France.

[63] D. Hernandez, J.L. Sans, M. Pfänder, Pyroreflectometry to determine the true temperature and optical properties of surfaces, *J. Sol. Energy Eng.* 130 (3) (2008) 031003, https://doi.org/10.1115/1.2840575.

[64] D. Hernandez, A. Netchaieff, A. Stein, True temperature measurement on metallic surfaces using a two-color pyroreflectometer method, *Rev. Sci. Instrum.* 80 (2009) 094903, https://doi.org/10.1063/1.3208011.

[65] D. Hernandez, J.L. Sans, A. Netchaieff, P. Ridoux, V. Le Sant, Experimental validation of a pyroreflectometric method to determine the true temperature on opaque surface without hampering reflections, Measurement 42 (6) (2009) 836–843, https://doi.org/10.1016/j.measurement.2009.01.012.

[66] H.R. Tschudi, M. Schubnell, Measuring temperatures in the presence of external radiation by flash assisted multiwavelength pyrometry, *Rev. Sci. Instrum.* 70 (1999) 2719–2727, https://doi.org/10.1063/1.1149835.

[67] H.R. Tschudi, G. Morian, Pyrometric Temperature Measurements in Solar Furnaces, *J. Sol. Energy Eng.* 123 (2) (2001) 164–170, https://doi.org/10.1115/1.1355035.

[68] I. Alxneit, Measuring temperatures in a high concentration solar simulator – Demonstration of the principle, *Sol. Energy* 83 (3) (2011) 516–522, https://doi.org/10.1016/j.solener.2010.12.016.

[69] D. Potamias, I. Alxneit, A. Wokaun, Double modulation pyrometry: A radiometric method to measure surface temperatures of directly irradiated samples, *Rev. Sci. Instrum.* 88 (2017) 095112, https://doi.org/10.1063/1.4987129.

[70] D. Potamias, I. Alxneit, E. Koepf, A. Wokaun, Double Modulation Pyrometry Applied to Radiatively Heated Surfaces With Dynamic Optical Properties, *J. Sol. Energy Eng.* 141 (1) (2018) 011003, https://doi.org/10.1115/1.4040842.

[71] D. Potamias, I. Alxneit, J.-L. Sans, E. Guillot, A. Wokaun, Assessment of Double Modulation Pyrometry as a diagnostic tool for use in concentrated solar facilities, *Sol. Energy* 174 (2018) 660–668, https://doi.org/10.1016/j.solener.2018.09.028.

[72] T. Sentenac, R. Gilblas, D. Hernandez, Y. Le Maoult, Bi-color near infrared thermoreflectometry: A method for true temperature field measurement, *Rev. Sci. Instrum.* 83 (2012) 124902, https://doi.org/10.1063/1.4769802.

[73] R. Gilblas, T. Sentenac, D. Hernandez, Y. Le Maoult, Quantitative temperature field measurements on a non-gray multi-materials scene by thermoreflectometry, *Infrared Phys. Technol.* 66 (2014) 70–77, https://doi.org/10.1016/j.infrared.2014.05.014.

[74] B. Jahne, Practical Handbook on Image Processing for Scientific and Technical Applications, Second Edition, CRC Press, 2004.

[75] Vaisala, Humidity conversions: Formulas and methods for calculating humidity parameters, https://www.vaisala.com/en/lp/make-your-job-easier-humidity-conversion-formulas, Last accessed 01/12/23.

[76] B.D. Maione, C. Baldridge, M.W. Kudenov, Microbolometer with a multi-aperture polymer thin-film array for neural-network-based target identification, *Appl. Opt.* 58 (27) (2019) 7285–7297, https://doi.org/10.1364/AO.58.007285.

[77] Spectral Science Inc., MODTRAN®, http://modtran.spectral.com/, Last accessed 01/12/23.

[78] A. Berk, P. Conforti, R. Kennett, T. Perkins, F. Hawes, J. van den Bosch, MODTRAN6: a major upgrade of the MODTRAN radiative transfer code, *SPIE Proc.: Algorithms and Technologies for Multispectral, Hyperspectral, and Ultraspectral Imagery* 30 (9088) (2014) 90880H, https://doi.org/10.1117/12.2050433.

[79] C. Gueymard, G. Lopez, I. Rapp-Arraras, Atmospheric transmission loss in mirror-to-tower slant ranges due to water vapor, *AIP Conf. Proc.* 2017 (1850) 140010, https://doi.org/10.1063/1.4984518.

[80] G. Lopez, C.A. Gueymard, J.L. Bosch, I. Rapp-Arraras, J. Alonso-Montesinos, I. Pulido-Calvo, J. Ballestrin, J. Polo, J. Barbero, Modeling water vapor impacts on the solar irradiance reaching the receiver of a solar tower plant by means of artificial neural networks, *Sol. Energy* 169 (2018) 34–39, https://doi.org/10.1016/j.solener.2018.04.023.

[81] F. Sakuma, M. Kobayashi, Interpolation equations of scales of radiation thermometers, Proceedings of TEMPMEKO 1996 (1996) 305–310.

[82] Hamamatsu, Image sensor module C16090-03, https://www.hamamatsu.com/us/en/product/optical-sensors/image-sensor/image-sensor-modules/C16090-03.html, Last accessed 01/12/23.

[83] Spectrogon, Narrow Bandpass Filters, https://www.spectrogon.com/products/optical-filters/spectrogon-ab/narrow-bandpass-filters/#of_target, Last accessed 01/12/23.

[84] OPTEC SRL, SWIR lenses, https://ir.optec.eu/index.asp, Last accessed 01/12/23.

[85] A.J. Kantor, A.E. Cole, Mid-latitude atmospheres, winter and summer, *Geogr. Ann., Ser. A* 53 (1962) (1962) 171–188, https://doi.org/10.1007/BF02007120.